Bone 177 (2023) 116920

Contents lists available at ScienceDirect

Bone

journal homepage: www.elsevier.com/locate/bone

Full Length Article

Composition and micromechanical properties of the femoral neck compact bone in relation to patient age, sex and hip fracture occurrence

Tatiana Kochetkova [a,*], Markus S. Hanke [b], Michael Indermaur [c], Alexander Groetsch [a], Stefan Remund [d], Beat Neuenschwander [d], Johann Michler [a], Klaus A. Siebenrock [b], Philippe Zysset [c], Jakob Schwiedrzik [a,*]

[a] Empa, Swiss Federal Laboratories for Materials Science and Technology, Thun, Switzerland
[b] Department of Orthopedic Surgery, Inselspital, University of Bern, Switzerland
[c] ARTORG Center for Biomedical Engineering Research, University of Bern, Switzerland
[d] Institute for Applied Laser, Photonics and Surface Technologies (ALPS), Bern University of Applied Sciences, Burgdorf, Switzerland

ARTICLE INFO

Keywords:
Hip fracture
Coxarthrosis
Aging
Micro-CT
Nanoindentation
Quantitative Polarized Raman spectroscopy
Femtosecond laser ablation
Micropillar compression
PCA
Naïve Bayes

ABSTRACT

Current clinical methods of bone health assessment depend to a great extent on bone mineral density (BMD) measurements. However, these methods only act as a proxy for bone strength and are often only carried out after the fracture occurs. Besides BMD, composition and tissue-level mechanical properties are expected to affect the whole bone's strength and toughness. While the elastic properties of the bone extracellular matrix (ECM) have been extensively investigated over the past two decades, there is still limited knowledge of the yield properties and their relationship to composition and architecture. In the present study, morphological, compositional and micropillar compression bone data was collected from patients who underwent hip arthroplasty. Femoral neck samples from 42 patients were collected together with anonymous clinical information about age, sex and primary diagnosis (coxarthrosis or hip fracture). The femoral neck cortex from the inferomedial region was analyzed in a site-matched manner using a combination of micromechanical testing (nanoindentation, micropillar compression) together with micro-CT and quantitative polarized Raman spectroscopy for both morphological and compositional characterization. Mechanical properties, as well as the sample-level mineral density, were constant over age. Only compositional properties demonstrate weak dependence on patient age: decreasing mineral to matrix ratio ($p = 0.02$, $R^2 = 0.13$, 2.6 % per decade) and increasing amide I sub-peak ratio $I_{\sim1660}/I_{\sim1683}$ ($p = 0.04$, $R^2 = 0.11$, 1.5 % per decade). The patient's sex and diagnosis did not seem to influence investigated bone properties. A clear zonal dependence between interstitial and osteonal cortical zones was observed for compositional and elastic bone properties ($p < 0.0001$). Site-matched microscale analysis confirmed that all investigated mechanical properties except yield strain demonstrate a positive correlation with the mineral fraction of bone. The output database is the first to integrate the experimentally assessed microscale yield properties, local tissue composition and morphology with the available patient clinical information. The final dataset was used for bone fracture risk prediction *in-silico* through the principal component analysis and the Naïve Bayes classification algorithm. The analysis showed that the mineral to matrix ratio, indentation hardness and micropillar yield stress are the most relevant parameters for bone fracture risk prediction at 70 % model accuracy (0.71 AUC). Due to the low number of samples, further studies to build a universal fracture prediction algorithm are anticipated with the higher number of patients ($N > 200$). The proposed classification algorithm together with the output dataset of bone tissue properties can be used for the future comparison of existing methods to evaluate bone quality as well as to form a better understanding of the mechanisms through which bone tissue is affected by aging or disease.

* Corresponding authors.
E-mail addresses: tatiana.kochetkova@empa.ch (T. Kochetkova), jakob.schwiedrzik@empa.ch (J. Schwiedrzik).

https://doi.org/10.1016/j.bone.2023.116920
Received 4 July 2023; Received in revised form 22 September 2023; Accepted 25 September 2023
Available online 26 September 2023

1. Introduction

Bone fragility poses a significant socioeconomic burden on modern societies worldwide. With increased longevity, bone fractures are bound to increase in number. According to the International Osteoporosis Foundation, fragility fractures in Europe are projected to increase by 23 %: from 2.7 million in 2017 to 3.3 million in 2030 [1]. Accordingly, the resulting annual fracture-related costs are expected to increase by 27 %. Accounting for much of the health care expenditures and mortality, hip and vertebral fractures are the two most serious types [1,2].

Fragility fractures result from low-energy trauma arising from the reduced load-bearing capacity of bone. Such fractures are the main consequence of osteoporosis [3,4] – a skeletal disorder characterized by low bone density and structural deterioration of the bone tissue [1,5–8]. Osteoporosis is referred to as a "silent disease" since it is often left undertreated and undetected until it manifests in the form of fracture [9,10].

Bone strength depends on both bone quantity and quality. The former is also known as bone mass or bone mineral density (BMD) and is the most common predictor for clinical fracture risk assessment [11]. Current clinical methods to assess bone health status fully or greatly depend on BMD measurements. However, these methods bear considerable errors in bone fracture prediction and are often only carried out after the bone fracture occurs [12]. On the other hand, emerging evidence suggests a significant influence of tissue quality on the whole bone strength [13–16]. Bone quality is a cumulative term that includes various parameters like metabolism, composition and microarchitecture, excluding BMD, that contribute to the overall fracture resistance [17–20]. There are several methods for evaluating bone quality, mostly laboratory-based [15]. Bone composition is commonly assessed through gravimetric analysis and/or spectroscopic methods (FTIR, Raman) [21], while bone microarchitecture and ultrastructure are often measured through different high-resolution imaging modalities (micro-CT, high-resolution peripheral QCT, NMR and MRI) [22]. Bone mechanical properties are being measured at the different length scales from the whole-bone and bulk tissue mechanical testing down to the lamellae levels. Direct measurements of bone fracture resistance include experiments on crack-initiation and crack-growth toughness [23]. Bone characteristics are co-dependent and it is important to assess bone structure-composition-properties relationship when investigating the influence of disease and/or aging on bone performance.

Bone is a fascinating biological material, combining strength and toughness with a low weight. At the lowest level, bone comprises organic and mineral phases (mainly collagen type I and hydroxyapatite crystals) with water inclusions. Both mineral and organic bone constituents contribute to the mechanical properties of bone tissue [24,25]. The mineral part of bone largely determines its stiffness [26], while the collagen part, together with bound water and non-collagenous proteins, is primarily responsible for bone toughness, i.e. the ability of bone to dissipate energy during overloading [27,28]. Besides the influence of the individual bone components, bone possesses a unique hierarchical arrangement, which contributes drastically to its outstanding mechanical and morphological properties [22,29,30].

Although more and more parameters linked to bone quality are investigated, to date, there is no universally accepted bone quality characteristic that can be used to assess bone health status. The main goal of this study was (i) to assess multimodal ECM bone properties at the femoral neck sites of patients who underwent a hip arthroplasty due to coxarthrosis or hip fracture and (ii) to examine any possible correlation between measured bone properties and patient clinical information (age, sex, hip fracture status). The novelty of the current study includes the multimodal characterization of the bone ECM, enhanced with micropillar compression and thus providing the first data on the microscale yield properties of the compact bone matrix for a large number of patients.

2. Materials and methods

2.1. Sample preparation

Human femoral neck slices were collected during total hip arthroplasty at the University Hospital of Bern (Switzerland) and Tiefenau Hospital (Switzerland), carried in the course from September 2018 to February 2022. A double osteotomy was done to extract a femoral neck slice of varying thickness of 3–10 mm. After extraction, samples were rinsed with Ringer's solution, dab dried, and stored in the freezer at −20 °C. The collection of samples and the corresponding patient information was done following the Ethical approval 2018-01815 of the Kantonale Ethikkommission Bern (Switzerland). Patient information in pseudonymized form was securely stored in the SharePoint server of the University Hospital of Bern. In total, 59 femoral necks were collected, of which 42 had intact inferomedial regions and were used for the current study. Ultimately, the patients' age varied from 45 to 89 y.o., with 19 females and 23 males.

A schematic of the sample preparation is shown in Fig. 1. Bone cortices from the inferomedial part of the frozen femoral necks were manually cut out with a hand saw. The extracted bone pieces of about 3-10 mm in height and 5 × 5 mm width × depth were mechanically cleaned with a scalpel and ultrasonic cleaner. Samples were then embedded in 10 % phosphate-buffered formalin solution at room temperature for at least two days, dehydrated with increasing ethanol concentrations (70–100 %), followed up by xylol and methylmethacrylate+dibutylphtalate (80 % + 20 %) solutions in the course of 7–10 days. Finally, samples were embedded in MMA (80 % methylmethacrylate + 20 % dibutylphtalate + 1 % perkadox) and left for polymerization at room temperature for at least two days.

The upper part of the embedded bone piece, closer to the femoral shaft, was further sectioned with a diamond-coated saw under constant

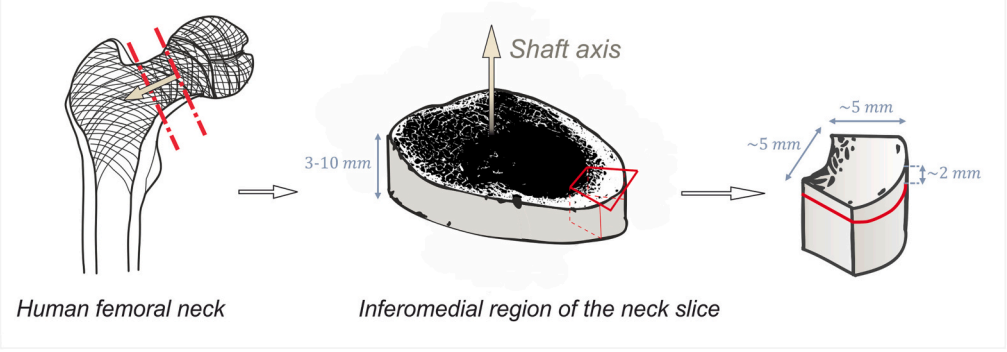

Fig. 1. Bone sample extraction and orientation schematic.

water irrigation. The resulting bone pieces of about 2 mm in height and 5 × 5 mm^2 area were then fixed onto an aluminum stub with a 2-component epoxy resin adhesive (Schnellfest, UHU, Germany). Finally, the exposed specimen surfaces were ultra-milled (Polycut E, Reichert-Jung, Germany) and consequently polished with 1000 grid silicon carbide and paper cloth with 0.3 μm Al_2O_3 slurry. The resultant surface roughness was below 50 nm, as assessed via an optical profilometer (S Neox, Sensofar Metrology, Spain).

2.2. Micromechanical characterization

2.2.1. Nanoindentation

Indentation maps were performed using a Zwick Roell nanoindenter system (ZHN Nanoindenter, ZwickRoell GmbH & Co. KG, Ulm, Germany) equipped with a Berkovich diamond tip. Indentation maps were distributed across the sample surface, each map was done within a bone structural unit (BSU) – single osteon or older interstitial tissue. In total, 20 bone BSU per patient were measured (Fig. 2), of which 10 were within osteonal and 10 in the neighboring interstitial regions. A 2 × 3 indentation map with 20 μm spacing was carried out in each BSU, resulting in 120 single indentations per patient. For each indent, a trapezoidal load control protocol was used [31] consisting of a loading segment at a rate of 1.5 mN/s, reaching up to 15 mN maximum force with about 1-1.2 μm penetration depth, holding for 5 s, and unloading at 3.75 mN/s. The penetration depth was estimated from the maximum force based on the setup calibration on the model materials (sapphire and fused silica) prior to the measurements. Bone tissue hardness and elastic modulus were calculated following the Oliver-Pharr method [32] with an assumed Poisson ratio of 0.3. Measurements were performed at room temperature and ambient pressure and humidity. Indentation maps were distributed across the sample surface, providing information on average elastic modulus and hardness at the whole sample level.

2.2.2. Micropillar compression

Regular arrays of bone micropillars were prepared on the sample surfaces following a previously developed femtosecond (fs) laser ablation protocol [33]. Micropillar fabrication was done using a 515 nm laser (SATSUMA HPII, Amplitudes Systemes) with 320–350 fs pulse duration, 3 kHz repetition frequency and 12 mW average laser power. This ablation protocol enables bone micropillar fabrication with low heat exposure (below the denaturation point of dry MCFs [33,34]), therefore minimizing any influence on the bone ECM. Since each sample presented a unique cortex morphology (varying cortical thickness and porosity), different combinations of micropillar arrays were fabricated across the sample surface: 5 × 9, 5 × 5, 4 × 5, 3 × 5, 3 × 10, 5 × 6 and 3 × 3. A scanning electron microscope image of the 4 × 5 micropillar array with a zoomed image of the single bone micropillar are shown in Fig. 3. As a result, each sample contained 45 to 65 bone micropillars, of which <8 % were a priori defective (fabricated fully or partially on Haversian canals or other pores). Micropillar geometry was assessed from each array on each sample via an optical profilometer (S Neox, Sensofar Metrology, Spain). On average, micropillars were 62 ± 2 μm high with a 26 ± 1 μm top diameter and 14 ± 2° taper (N = 1441).

Micropillar compression experiments were performed using an *ex situ* indenter setup developed in-house based on commercial hardware for actuation, sensing, and electronics (Alemnis AG, Switzerland) [35,36]. Experiments were performed at ambient temperature and humidity with a flat punch indenter tip (60 μm diameter). Samples were compressed uniaxially using a quasi-static displacement-controlled loading protocol at a strain rate of 10^{-3} s^{-1} and up to 13 % of engineering strain. As output, yield stress and strain values were extracted at 0.2 % plastic deformation. A schematic stress-strain curve of the bone micropillar is shown in Fig. 2. Per each sample, 30 to 50 micropillars were tested.

Data analysis was done in Python v3.8 [37] using an in-house script [33,38] following the methodology of Schwiedrzik et al. [31] with the modified Sneddon approach of Zhang et al. [39] for substrate compliance corrections. The influence of the taper angle on the output mechanical properties was corrected using finite element simulations in Abaqus/CAE (Dassault Systemes Simulia Corp., Johnston, Rhode Island, USA) [40] following our previous work [33].

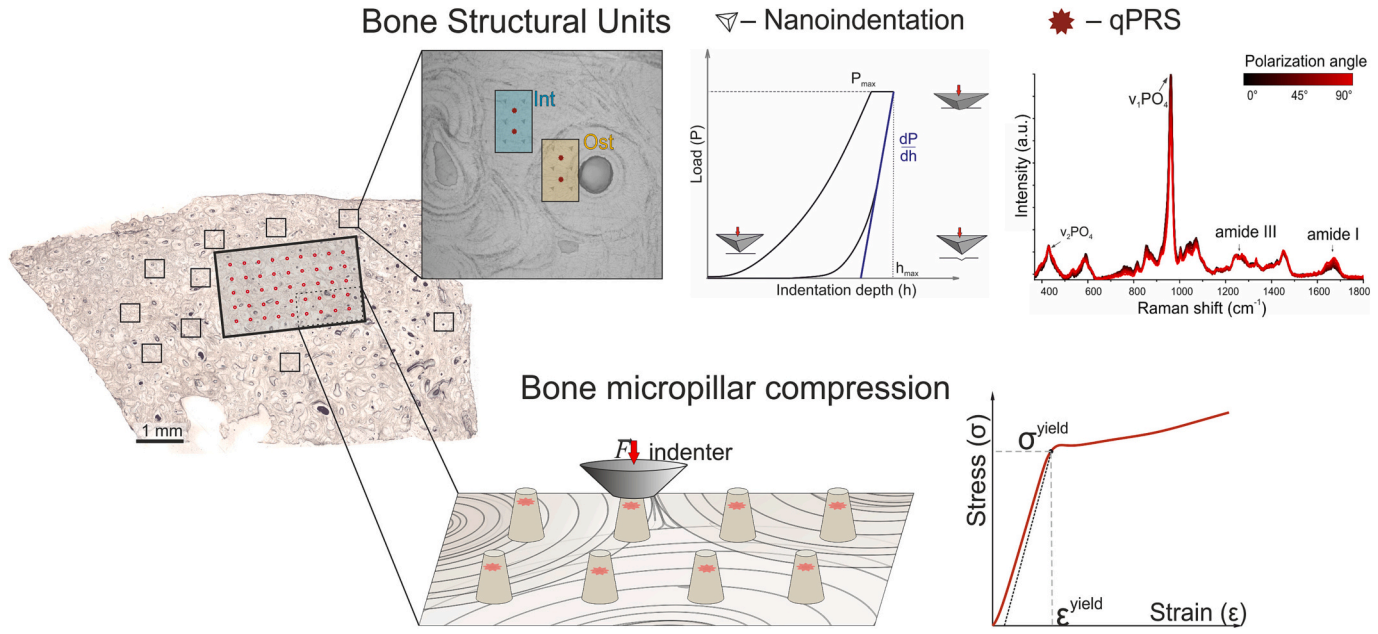

Fig. 2. Microscale analysis methods and their schematic location on the sample surface. The whole sample volume was scanned with micro-CT. Structural unit analysis on interstitial (Int) and osteonal (Ost) zones included nanoindentation maps and quantitative polarized Raman spectroscopy (qPRS) measurements within the mapping area. A typical indentation curve and polarized Raman spectra are shown at the top right. A schematic of the bone micropillar compression is shown at the bottom. Compression tests were site-matched with qPRS measurements on each pillar. A typical stress-strain curve from the micropillar compression experiment is shown at the bottom right.

2.3. Morphological and compositional analysis

2.3.1. Micro-CT

Hydroxyapatite-calibrated micro-computed tomography (micro-CT) scans of the whole sample volume were collected for each sample prior to mechanical measurements. Scanning was done at 55 kVp energy, 200 μA tube current, and 300 ms integration time, with a resulting voxel size of 17.2 μm (microCT 100, SCANCO Medical AG, Switzerland). Following the reconstruction, image processing was done using in-house Matlab code (Matlab R2019a). A schematic of the image processing steps is shown in Appendix A, Fig. A1. For each sample, cortical bone mineral density (BMD, computed as the average of the hydroxyapatite-calibrated grey values of the scanned bone volume), tissue mineral density (TMD, computed as the average of the masked grey values of the scanned bone volume) and bone volume ratio (BV/TV, bone volume vs. the total volume) were extracted.

2.3.2. Quantitative polarized Raman spectroscopy (qPRS)

Raman spectra were acquired in ambient conditions via an upright Raman microscope (Nova Spectra, ND-MDT, Russia) with a 633 nm laser. The linear polarization of the exciting laser was adjusted with a motorized λ/2 plate. No analyzer plate was included in the light path after the sample. Spectra were collected using a 600 g/mm grating and 50× objective with a numerical aperture of 0.55. The resultant focal range of the laser was ~0.7 μm in the lateral and 4.2 μm in the axial direction [41]. The laser power at the sample surface was ~7 mW.

Two sets of measurements were collected for each sample. First, polarized spectra were acquired from bone structural units within interstitial and osteonal regions after the nanoindentation tests. Two sets of spectra were collected from the central region of the indentation map, ~10 μm away from the neighboring indents, to avoid measuring indented bone volume (Fig. 2). The second set of measurements was done within each bone micropillar before compression tests, approximately 5 μm underneath the pillar top surface. Each set of polarized Raman measurements consisted of 10 spectra, collected at increasing polarizer angles from 0 to 180° with a 20° angular step. The local orientation of the mineralized collagen fibrils (MCF) was estimated following a previously reported qPRS method [35]. Local in- and out-of-plane MCF angles were calculated and used for the subsequent correlation analysis. Moreover, traditional information on the bone microscale composition was quantified through the peak band ratios.

The peaks of interest were chosen based on the principal component analysis [42]. For this, all spectra were background subtracted and averaged spectra from all samples were analyzed. The peaks with the highest intensities variation were detected as elements from the first eigenvector (principal component) after the dimensionality reduction. The peaks with the highest variation included primary and secondary phosphate (v_1PO_4, v_2PO_4), proteoglycans, and collagen bands (amide I

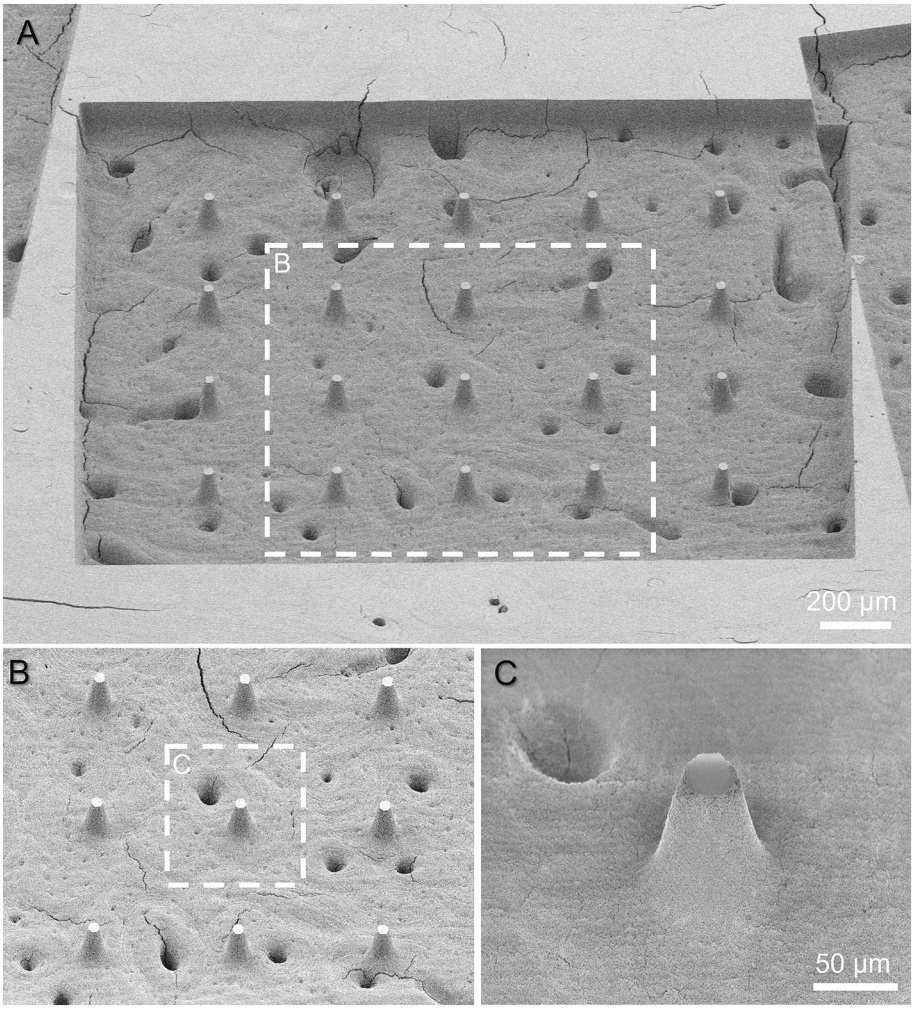

Fig. 3. Scanning Electron Microscope images of the bone micropillar array. A – array of 4 × 5 bone micropillars fabricated via femtosecond laser ablation, note the ablated regions of neighboring micropillar arrays on both sides. B – zoomed image of the central pillars marked in panel A, note the bone surface cracks due to the high vacuum exposure. C – zoomed image of the single bone micropillar next to the Haversian canal. Note that the Haversian canals seem empty because the surface ablation with the laser eroded MMA at a higher rate than bone. All images were taken after the experimental campaign to avoid sample exposure to a vacuum.

Table 1
Bone compositional and structural parameters assessed via Polarized Raman spectroscopy.

Parameters		Quantification of the parameters	Interpretation
1	Mineral to matrix ratio	Integrated area of v_2PO_4 (410–460 cm^{-1}) over amide III (1215–1300 cm^{-1})	Relative mineralization level. Correlates with Ca content [43]
2	Mineral crystallinity index	Inverse value of v_1PO_4 full width at half maximum	Mineral crystallite chemistry, size and shape [44,45]
3	Amide I sub-peak ratio $I_{\sim1670}/I_{\sim1640}$, collagen disorder/order ratio	Intensity ratio of amide I sub-bands: $I_{\sim1670}/I_{\sim1640}$	Collagen helical structure disorderliness [46,47]
4	Amide I sub-peak ratio $I_{\sim1660}/I_{\sim1683}$, matrix maturity ratio	Integrated area ratio of amide I sub-bands: $I_{\sim1660}/I_{\sim1683}$	Nonquantitative measure of cross-link maturity [47–49]
5	MCF in- and out-of-plane orientation	Integrated area ratio of amide I (1215–1300 cm^{-1}) over amide III (1600–1700 cm^{-1})	MCF spatial orientation [35]

and amide III). Accordingly, the compositional parameters presented in Table 1 were extracted from the Raman spectra. The corresponding peaks were background subtracted and fit with a linear combination of Lorentzian functions [33,35]. The results from each measured ROI were averaged over the laser polarizations to exclude the polarization dependence from the analyzed parameters (1-4, Table 1).

2.4. Statistical analysis

Descriptive statistics and correlation analysis were performed in R v.4.2 [50] with the rstatix [51], lme4 [52], lmerTest and lmtest packages. The Shapiro-Wilk test and QQ plots were used to verify the normality of variables. A mixed-effect model was used to account for the repeated tests per sample and within the bone structural units (BSU) of each sample. For this, groups (sex, diagnoses, zones) and patient's age were treated as fixed effects, while samples and bone structural units (within interstitial or osteonal zones) within the samples were taken as random effects (Eq. (1)). The influence of the group, age and their interaction on the measured variables was accounted for in the model:

$$variable \sim Group^{*}Age + (1|Sample) + (1|BSU : Sample). \quad (1)$$

The likelihood ratio test confirmed that the random effects significantly influence the model for all of the measured variables. Differences in the mean between the groups were tested using the one-way ANOVA test with the mixed model (1), F-statistic was computed with Satterthwaite's method, the significance threshold was chosen as $p < 0.05$. Mean and standard deviation (SD) are reported. Linear correlation of the measured variables from the patient's age was combined with the mixed effect model, similar to the group analysis:

$$variable \sim Age + (1|Sample). \quad (2)$$

A multiple regression analysis was used to check the correlation between measured bone properties (Python's NumPy module [53]) using Pearson correlation coefficients as a correlation matrix.

A principal component analysis (PCA) was carried out on the final dataset combining the mean of the measured bone parameters per each sample with the clinical information for each patient. PCA was done in Python v.3.9 [37] via the Scikit-learn machine learning library [54]. Gaussian Naïve Bayes analysis (Scikit-learn) was applied to predict fractured and non-fractured patients [55]. The final dataset was transformed to avoid categorical inputs and split into training and test sets with a 0.75 to 0.25 ratio, respectively. The model accuracy was calculated as the fraction of the correct predictions, defined as the ratio of true positives and true negatives to all observations. Area Under the Curve (AUC) of the Receiver Operating Characteristic (ROC) was additionally used to assess the classifier performance.

3. Results

3.1. Sample cohort description

In total, 42 patients participated in this study, with age varying from 45 to 89 y.o. (Fig. 4). A fair distribution of patients' age and sex was observed, with a close number of female and male patients: 19 and 23, respectively (Fig. 4A). Following the clinical information about the patient's primary diagnosis, samples were assigned to one of the two

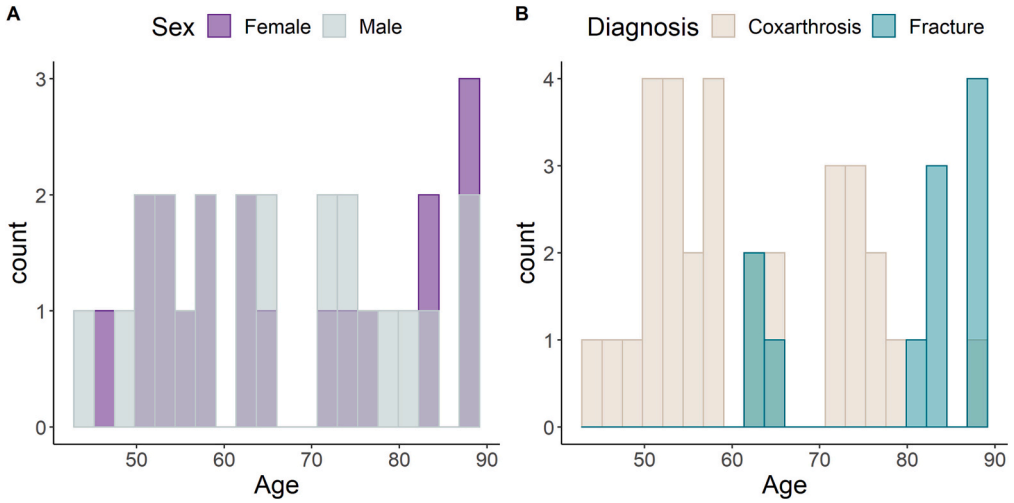

Fig. 4. Histogram of patients' sex (A) and primary diagnosis (B) distributions across the age. In total, 42 patients participated in this study. Female: N = 19, mean age 67 years. Male: N = 23, mean age 66 years. Patients with coxarthrosis: N = 31, mean age 62 years. Patients with hip fracture: N = 11, mean age 79 years.

groups: coxarthrosis (N = 31), where patients suffered from hip osteoarthritis but had no clinical record of the metabolic bone disease, and fracture patients (N = 11), who had to be operated due to hip fractures (Fig. 4B). Such fractures in the context of low-energy trauma are considered the most severe complication of osteoporosis. While the fracture patients were not formally diagnosed with osteoporosis, we consider them patients at high risk of osteoporosis. Hip fractures were only observed in patients aged 60 years and above.

3.2. Bone properties in relation to patient sex, diagnosis and age

A summary of measured bone properties depending on the patients' cohorts is collected in Table 2.

Neither elastic nor yield properties of bone tissue demonstrate any dependence on the patients' age (Fig. 5). The same is true for the bone mineral densities and the volumetric ratio. Only local bone composition demonstrates a marginal correlation with the patient's age. Notably, the mineral to matrix ratio declines with age ($p = 0.02$, $R^2 = 0.13$, 2.6 % per decade), while the amide I sub-peak ratio $I_{\sim1660}/I_{\sim1683}$, also referred to as matrix maturity ratio, increases ($p = 0.04$, $R^2 = 0.11$, 1.5 % per decade).

Hip fracture occurrence did not seem to affect any of the investigated bone properties. The same is true for the patient sex – no significant difference in bone material properties was observed between the female and male patients. Patients with hip fractures were, on average, 18 years older than the patients with coxarthrosis (Fig. 4). To exclude the bias related to the age difference from the grouped comparison (sex, diagnosis, zone), the influence of age was corrected for all of the measured bone properties (Eq. (1)).

Zonal dependence between investigated bone structural units was observed for mechanical and a subset of compositional characteristics (Fig. 5). Specifically, the mineral to matrix ratio was on average 5 % higher in the interstitial zone than in the osteonal ($p < 0.0001$). Meanwhile, the amide I sub-peak ratio $I_{\sim1670}/I_{\sim1640}$ (collagen disorder/order ratio) was 1.2 % higher in the osteonal bone region ($p < 0.0001$). As for the micromechanical properties, both elastic moduli and hardness of interstitial zones were on average 1.4 % and 2.6 % higher than those of osteonal zones ($p < 0.0001$).

3.3. Compact bone structure-properties relationship

Investigated mechanical properties of compact bone exhibited positive correlation with the tissue mineralization levels (Fig. 6). Average sample hardness and yield stress positively correlated with bone tissue mineral density ($p < 0.02$). No dependence was observed for the averaged elastic moduli ($p > 0.6$).

The site-matched analysis of microscale mechanical, compositional and morphological properties allows for quantifying compact bone's local structure-properties relationships. Both elastic moduli and hardness positively correlated with the mineral to matrix ratio ($p = 2.9 \cdot 10^{-9}$, $R^2 = 0.042$ and $p = 8 \cdot 10^{-5}$, $R^2 = 0.019$, respectively). The statistical significance reduces for the patients with hip fractures: $p = 0.16$ for E and $p = 0.026$ for H versus $p < 0.0001$ for both E and H of coxarthrosis patients. Most likely, this is due to the smaller sample size: 11 patients with hip fractures versus 31 coxarthrosis patients. The same positive correlation with the mineral to matrix ratio was observed for the local yield stress ($p < 2.2 \cdot 10^{-16}$, $R^2 = 0.062$). This correlation remains for both coxarthrosis ($p = 1.9 \cdot 10^{-10}$, $R^2 = 0.037$) and fracture patients ($p = 1.8 \cdot 10^{-13}$, $R^2 = 0.15$) (Fig. 6). Besides local mineralization levels, out-of-plane MCF orientation was measured following the qPRS method. Neither elastic nor yield micromechanical properties significantly correlated with the MCF out-of-plane angle ($p = 0.45$, $p = 0.82$, respectively).

3.4. Overall correlation between measured bone properties

A multiple regression analysis was carried out to assess the overall correlation between measured bone properties. Pearson correlation matrix, shown in Fig. 7, summarizes the output correlation coefficients r, where $r \to 0$ for a dismal correlation and $r \to 1/-1$ suggests a distinct positive/negative correlation between the parameters. The significant correlations ($p \leq 0.05$) are additionally highlighted with the black frame. Note that the presented analysis was carried out on the averaged bone properties per patient; therefore, the correlation results are somewhat different from the site-matched analysis.

Overall, the mineral to matrix ratio and, marginally, the yield stress values averaged per patient demonstrate a negative correlation with the patient's age ($r = -0.4$ and $p = 0.02$, $r = -0.2$ and $p = 0.04$, respectively). Elastic moduli correlate strongly with hardness ($r = 0.86$, $p < 0.0001$), as expected from the methodology [56], while a moderate correlation with the yield stresses is observed ($r = 0.47$, $p = 0.03$).

As shown in Fig. 7, local crystallinity increases with the local mineral to matrix ratio ($r = 0.7$, $p = 0.001$) and marginally decreases with the sample-level TMD ($r = -0.1$, $p = 0.01$) and BMD ($r = -0.2$, $p = 0.01$). Interestingly, local crystallinity correlates positively with the amide I sub-peak ratio $I_{\sim1670}/I_{\sim1640}$ (collagen dis./order ratio, $r = 0.7$, $p < 0.001$), suggesting a hidden interplay of mineral and organic bone fractions. Mineralized collagen fibrils' out-of-plane orientation correlates with the mineral to matrix ratio ($r = -0.4$, $p = 0.02$). However, this is likely due to the Raman ratio's quantification similarities since both of these Raman parameters depend on the amide III integral area.

3.5. Prospective bone fracture biomarkers

A principal component analysis (PCA) was employed to define a combination of bone parameters measured in this study, which would explain the observed variations in bone properties. It allowed us to reduce the data's dimensionality by defining linear combinations of bone properties, acting as new eigenvectors (principal components) for our multidimensional dataset. Eight variables were included in the PCA: patients' age, bone hardness, yield stress and strain, mineral to matrix ratio, amide I sub-peak ratios, and TMD. According to the PCA, the first two principal components could explain ~45 % of observed variations between the patients (Appendix B, Fig. B1).

Four classification algorithms were tested on the PCA-processed final data with reduced collinearity: logistic regression, support vector machines, Gaussian Naïve Bayes and *k*-nearest neighbor. The classifiers were chosen based on their applicability to the medical diagnosis [57–59], especially osteoporosis prediction [60]. With the training-to-test dataset ratio of 0.75:0.25, the dataset from 32 patients was used to train the model, while the remaining 10 were used to evaluate the models' performances. The model accuracy was calculated as the fraction of the correct predictions, defined as the ratio of true positives and true negatives to all observations. The first three classification algorithms showed matching accuracy scores of 0.7, while KNN was only able to reach a 0.5 score (Appendix B, Fig. B2). The receiver operating characteristic (ROC) curve with the area under the curve (AUC) measure allowed us to assess the classifier performance further. The Gaussian Naïve Bayes algorithm reached the highest AUC score of 0.71, while logistic regression and support vector machines only reached a 0.52 AUC score. Accordingly, the Naïve Bayes algorithm was chosen for the final data classification. As a result, the variables that contributed the most to the fracture predictions were the mineral to matrix ratio, micropillar yield stress and indentation hardness. Exact scores as well as the model confusion matrix can be found in Appendix B, Fig. B3.

4. Discussion

In this study, microscale elastic and yield mechanical properties, as well as bone composition and morphology, were assessed in 42 aging

Table 2
Summary of measured bone properties depending on the patients' sex, diagnosis or zone. p-values from the one-way ANOVA test with the nested mixed effect model of the bone characteristics compared within mentioned cohorts of patients. p-values for the group (sex, diagnosis or zone), age and their interaction (interact.) are reported.

Method	Bone characteristics	Sex			Diagnosis			Zone		
		Female (N = 19)	Male (N = 23)	p-values	Coxarthro-sis (N = 31)	Fracture (N = 11)	p-values	Interstitial (N = 42)	Osteonal (N = 42)	p-values
Nanoindentation	E, GPa	22.0 ± 2.3	21.5 ± 2.3	0.95 (group) 0.74 (age) 0.65 (interact.)	21.77 ± 2.3	21.6 ± 2.3	0.35 (group) 0.54 (age) 0.31 (interact.)	21.9 ± 2.4	21.6 ± 2.3	**<0.0001 (group)** 0.79 (age) **0.001 (interact.)**
	H, MPa	716.7 ± 88.5	706.2 ± 90.4	0.99 (group) 0.38 (age) 0.81 (interact.)	710.7 ± 89.7	711.3 ± 90.0	0.33 (group) 0.87 (age) 0.28 (interact.)	721.3 ± 88.3	702.3 ± 90.2	**0.001 (group)** 0.36 (age) 0.11 (interact.)
Micropillar compression	Yield stress, MPa	263.6 ± 38.5	252.2 ± 41.9	0.41 (group) 0.11 (age) 0.27 (interact.)	259.3 ± 41.8	251.1 ± 36.8	0.86 (group) 0.46 (age) 0.89 (interact.)	–	–	–
	Yield strain, -	0.033 ± 0.004	0.033 ± 0.005	0.11 (group) 0.67 (age) 0.10 (interact.)	0.033 ± 0.004	0.033 ± 0.005	0.74 (group) 0.73 (age) 0.70 (interact.)	–	–	–
Micro-CT	BMD, mg/cm^3	1000.7 ± 40.4	1007.0 ± 41.0	0.62 (group) 0.42 (age) 0.58 (interact.)	999.4 ± 36.1	1019.4 ± 51.0	0.17 (group) 0.96 (age) 0.16 (interact.)	–	–	–
	TMD, mg/cm^3	1032.4 ± 35.7	1035.9 ± 33.7	0.75 (group) 0.17 (age) 0.89 (interact.)	1029.3 ± 29.6	1050.2 ± 44.1	0.09 (group) 0.65 (age) 0.24 (interact.)	–	–	–
	BV/TV, %	95 ± 2	96 ± 2	0.64 (group) 0.42 (age) 0.25 (interact.)	96 ± 2	96 ± 2	0.99 (group) 0.29 (age) 0.20 (interact.)	–	–	–
Raman Spectroscopy	Mineral/Matrix ratio	0.69 ± 0.12	0.66 ± 0.12	0.54 (group) 0.026 (age) 0.74 (interact.)	0.69 ± 0.12	0.63 ± 0.11	0.51 (group) 0.58 (age) 0.62 (interact.)	0.63 ± 0.10	0.60 ± 0.10	**<0.0001 (group)** **0.006 (age)** **<0.0001 (interact.)**
	Mineral crystallinity index	0.0635± 0.0012	0.0631± 0.0011	0.57 (group) 0.75 (age) 0.41 (interact.)	0.0634± 0.0011	0.0630± 0.0011	0.34 (group) 0.34 (age) 0.43 (interact.)	0.0636± 0.0011	0.0628± 0.0012	**0.0001 (group)** 0.92 (age) **0.009 (interact.)**
	$I_{\sim1670}/I_{\sim1640}$, collagen disorder/order ratio	1.70 ± 0.09	1.69 ± 0.07	0.66 (group) 0.38 (age) 0.61 (interact.)	1.70 ± 0.08	1.68 ± 0.08	0.60 (group) 0.12 (age) 0.78 (interact.)	1.67 ± 0.08	1.69 ± 0.08	**<0.0001 (group)** 0.29 (age) **0.014 (interact.)**
	$I_{\sim1660}/I_{\sim1683}$, matrix maturity ratio	1.42 ± 0.10	1.42 ± 0.10	0.22 (group) 0.06 (age) 0.20 (interact.)	1.40 ± 0.09	1.47 ± 0.09	0.42 (group) 0.20 (age) 0.30 (interact.)	1.45 ± 0.11	1.43 ± 0.11	0.10 (group) **0.03 (age)** **0.019 (interact.)**

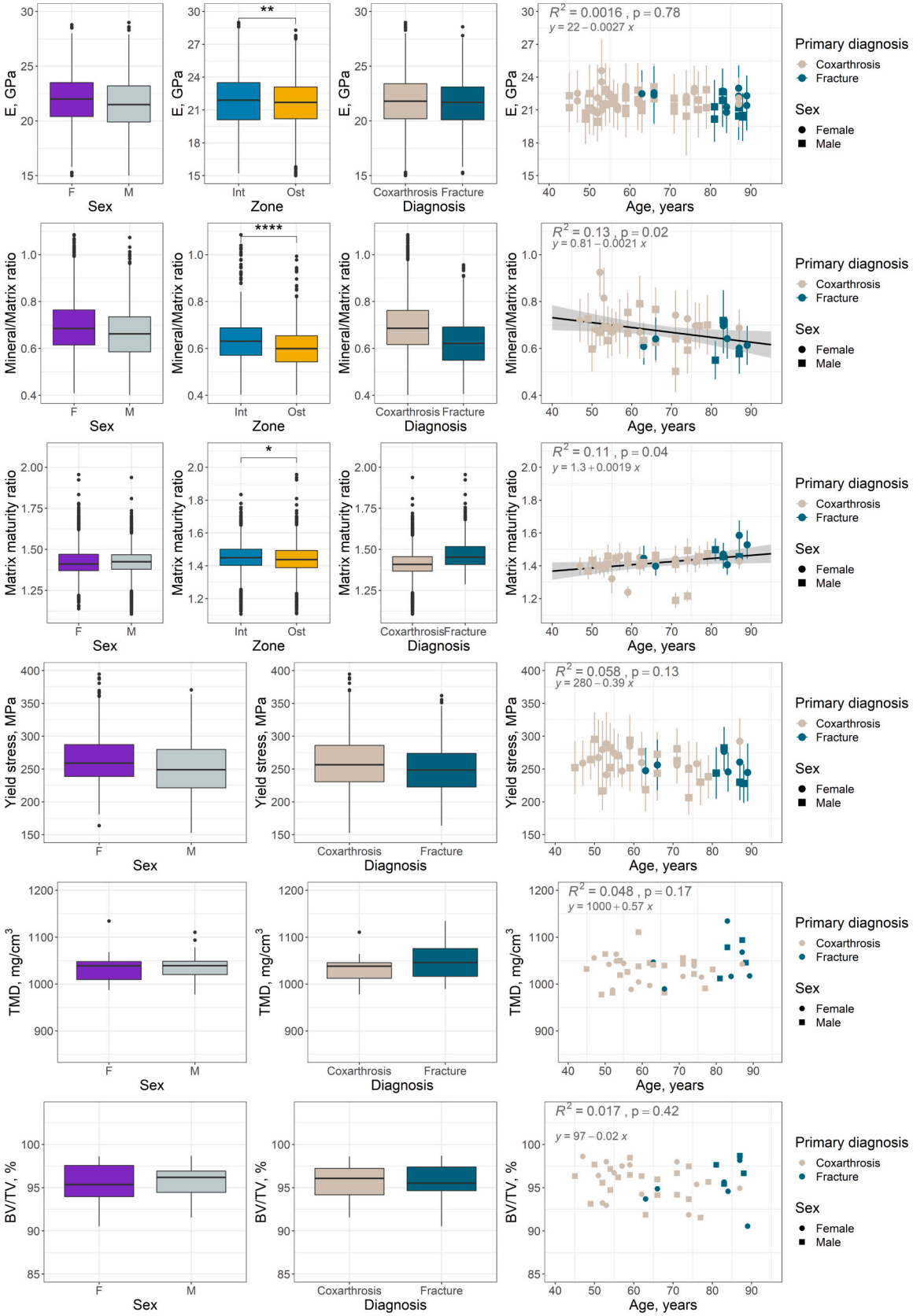

Fig. 5. Compact bone properties in relation to the patient sex, primary diagnosis, age and analyzed cortical bone zone (interstitial, osteonal). Measured bone propertied from top to bottom: elastic moduli (E), mineral to matrix ratio (mineral/matrix ratio), $I_{\sim 1660}/I_{\sim 1683}$ (matrix maturity ratio), yield stress, tissue mineral density (TMD) and bone volume fraction (BV/TV). Statistical significance asterisks: * – $p \leq 0.05$, ** – $p \leq 0.01$, *** – $p \leq 0.001$, **** – $p \leq 0.0001$.

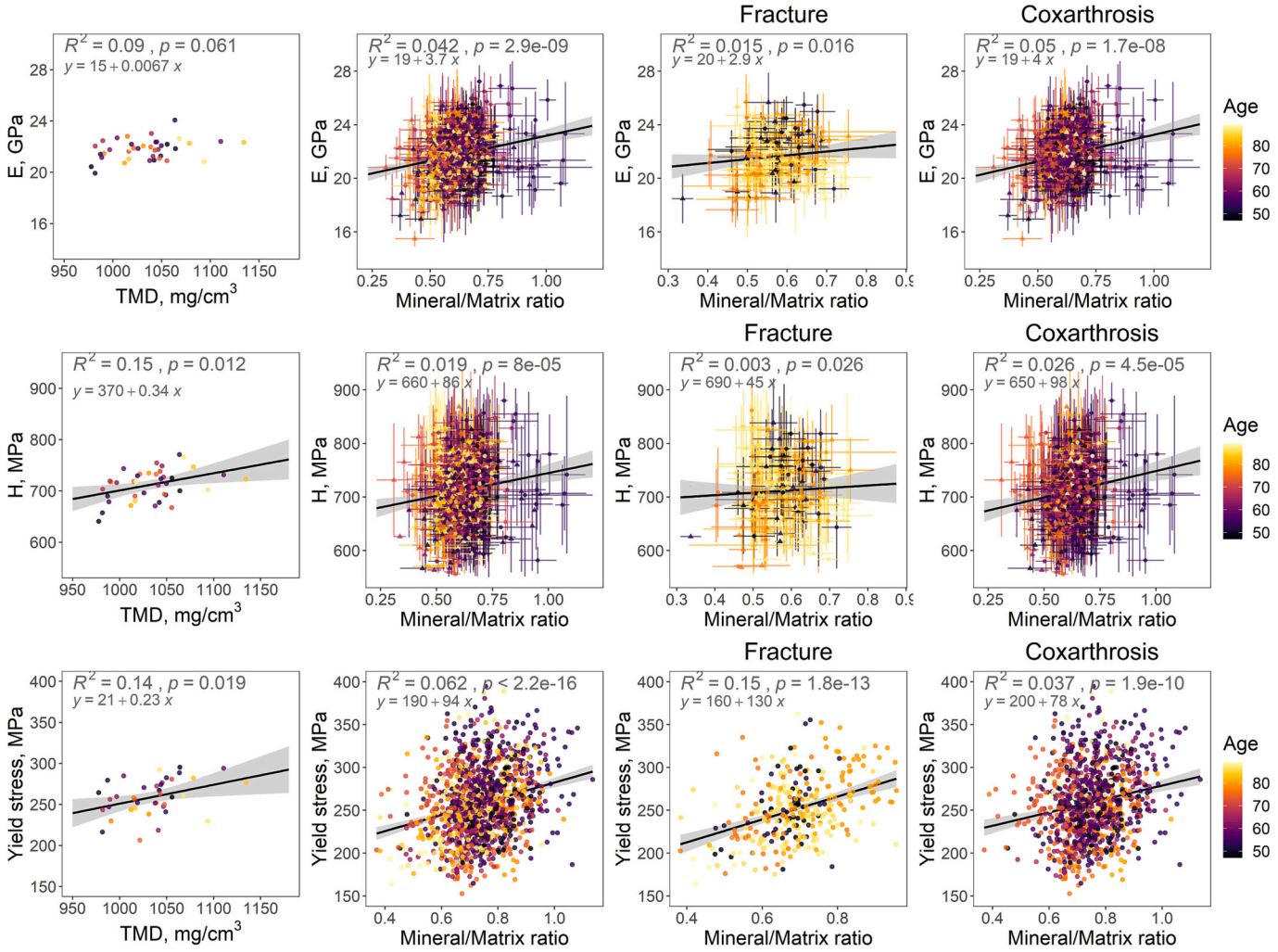

Fig. 6. Local mineral-mechanical relationships of compact bone in relation to the patient's age and primary diagnosis.

patients. All measurements were done *ex vivo* using laboratory-based methods for morphological, compositional, and micromechanical compact bone properties assessment. The collected experimental data included compact bone tissue mineral density and volumetric fraction, measured via micro-CT. Compositional properties related to mineral and organic content were assessed via polarized Raman spectroscopy, and microscale elasto-plastic mechanical properties were measured via nanoindentation and micropillar compression techniques. The output collection of bone properties was combined with the clinical information about the patient's age, sex and primary diagnosis, including the incidence of the hip fracture. Statistical analyses within the collected data frame as well as between the site-matched bone properties were performed with the aim of better understanding the structure-mechanical property relationships in a human compact bone at the microscale and identifying prospective bone parameters related to bone fracture. The measured database of bone tissue properties together with the patient information allowed us to run the *in-silico* fracture prediction algorithm based on Naïve Bayers classification of the PCA-processed data. To our knowledge, this is the first study where supervised machine learning algorithms are applied to the multimodal dataset of bone ECM properties with an attempt to define perspective markers of bone quality. The described approach can be used in future multimodal studies on bone quality assessment and correlation to the clinical methods of fracture risk prediction.

4.1. *Microscale bone mechanical properties*

The elastic moduli of the cortical bone regions of the femoral necks investigated in this study varied from 15 to 28 GPa between the patients. Similarly, hardness values from 530 to 880 MPa were observed. This agrees with independently reported nanoindentation data on the human femur with elastic moduli of approximately 16 to 28 GPa [56,61–64] and about 300 to 760 MPa hardness values [61,65,66]. High variation within the inferomedial region may be due to inherited bone tissue heterogeneity. In future studies, taking into account the periosteum-endosteum localization, besides osteonal-interstitial zonal variations, would help to reduce the macroscopically induced variations of the tissue level properties.

Patients with hip fractures exhibited comparable microscale bone hardness and elastic moduli as that of coxarthrosis patients. Moreover, neither patient's age nor sex had a significant influence on the microscale mechanical properties. A similar absence of correlation between the elastic properties and the fracture status of the femoral necks was shown by Fratzl-Zelman et al. [62] for the femoral neck samples from elderly female patients. In another study by Mirzaali and Schwiedrzik et al. [67], indentation measurements were done on proximal femurs from donors of age 46-99, and microindentation properties were shown to be constant over age and not sex-dependent. Jenkins et al. found a 7 % reduction in fracture toughness per decade for the cortical bone at the inferomedial femoral neck but no influence of osteoporosis or osteoarthritis [68]. In a more recent study by Bonicelli et al., lamellar bone

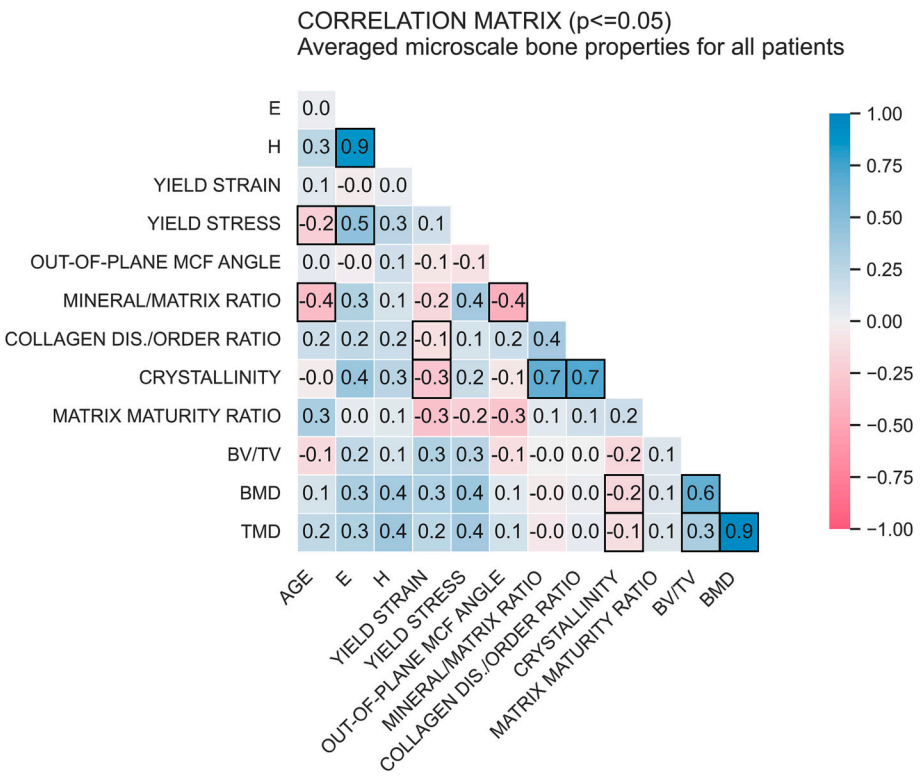

Fig. 7. Pearson's correlation coefficients (r) from the multiple regression analysis of the averaged bone properties for all patients. Significant correlations ($p \leq 0.05$) are marked with the black frame.

hardness of the femoral head was found to be lower for donors with hip fractures [69].

While nanoindentation is a commonly used laboratory-based method of bone mechanical properties analysis [56], micropillar compression studies are scarce. Indeed, the micropillar compression technique requires the time-consuming preparation of bone micropillars [31,36,70–73], in contrast to the plain polished surface that is required for the nanoindentation measurements. On the other hand, micropillar compression can provide information not only on bone elastic properties but also on yielding and post-yielding behavior. In the current study, we employed a recently developed laser ablation protocol for fast and repeatable micropillar fabrication [33]. A similar approach was developed for *in situ* micromechanical testing at synchrotrons, but the authors used an additional ion-beam-based preparation step to create the final micropillars [72]. From our estimations, bone surface temperature during ablation should not exceed 80 °C [33], which is below the denaturation point of dry collagen [34], but may still affect the collected Raman spectra [74]. The laser ablation procedure presented here allowed us to carry out a high-throughput micropillar compression study, approaching the measurement rate of the nanoindentation method.

This is the first study where high-throughput micropillar compression experiments (N = 1441) were carried out on a large number (N = 42) of human cortices. Consequently, we cannot directly compare measured microscale yielding bone properties at the femoral neck site with other studies. Observed yield stress values varied from 206 to 295 MPa between the patients. That is above previously reported values for the macroscopic compressions of the femur diaphysis cortical bone (148 ± 16 MPa) [67], highlighting the "smaller is stronger" effect in bone [31]. On the other hand, yield stress values assessed in the present work are somewhat lower than available data on micropillar compression of femoral condyle trabecular bone (313–327 MPa, 3 μm pillar diameter [71]) or iliac crest cortex (~350 MPa, 5 μm pillar diameter [70]). However, as was nicely demonstrated by Tertuliano and Greer [71], micropillar size drastically affects the output properties since different levels of hierarchy are being tested. As a tradeoff for the high-throughput measurements, laser-ablated micropillars had a bigger size (almost five times larger diameter than in previously reported studies [31,35,36,70,71,73]) and a taper, which influence was accounted for through the use of finite element simulations [33]. Consequently, a larger number of material defects like lacunae or lamellae interfaces are present within the micropillar. An even more drastic decrease in strength values with the specimen size was observed by Casari et al. [75] during microscale tensile testing.

Microscale yield stress values were consistent between female and male patients across investigated ages (45–89 y.o.). The occurrence of the hip fracture also seems to not affect the compressive yield stress and strain at this scale, although the tensile failure strain is reported to be lower for the fractured donors at the femoral head trabeculae [69].

Mechanical tests were carried out at ambient temperature and humidity. This, together with the tissue fixation procedure might have diminished age-related differences in mechanical properties. Microsamples in fully wet conditions swell and deviate from the *in situ* boundary conditions desired for homogeneous stress/strain distributions during relevant mechanical tests [73]. Micropillar compression in wet conditions may introduce a new bias in the detection of age-related differences and computational methods to overcome this conundrum are endorsed.

4.2. Bone composition and morphology

Tissue mineral density values assessed in the current work were in line with available studies (868–1020 mgHA/cm^3 [76,77]). Bone volume fraction levels are similar to reported measurements, reaching up to 99 % of BV/TV (1 % porosity [77]). However, we are likely not able to segment the smaller pores like lacunae with the available resolution (17.2 μm voxel size). Bone density (BMD, TMD) as well as the bone volume fraction were consistent between the patients' cohorts (both sex,

both diagnoses) and were seemingly constant across the investigated ages. On the contrary, Voumard et al. observed decreased aBMD as well as bone volume fraction with the donor's age [76]. Most probably, we do not observe any correlation with age because we only measured the inferomedial region of the femoral neck, in contrast to the whole neck slice [76]. Indeed, geometrical features at the femoral neck, especially cortical bone thickness, contribute drastically to hip fracture occurrence [78]. Thus, bone fractures might be a result of a complex interplay of tissue properties with geometrical features.

Bone compositional parameters, as assessed via quantitative Polarized Raman spectroscopy, were in line with previously reported values on human femurs: 0.4–1.6 mineral to matrix ratio [43], 1.35–1.60 amide I sub-peak ratio $I_{\sim1670}/I_{\sim1640}$ [46,47]. Available data on the Raman $I_{\sim1660}/I_{\sim1683}$ ratio is only reported for the young mice models: 1.9–2.5 [48]. We observed marginally increased mineral crystallinity values (0.065 in comparison to 0.05–0.06 in other works [67,79,80]), which may indicate changes in the strain environment of the lattice possibly caused by the sample fixation and embedding procedure [81]. As anticipated, clear zonal dependence is present for investigated compositional parameters. More specifically, interstitial bone regions exhibit 5 % higher mineral to matrix ratios, similar to other studies [27,80]. Mandair et al. used the ratio of v_3PO_4/v_1PO_4 (I_{1044}/I_{956}) as a metric for lamellar organization, which could additionally be used in the future to assess the differences in organization between interstitial and osteonal bone [82]. Averaged mineral to matrix ratios did not correlate with sample level TMD, most likely due to the small range of both parameters and different physical meaning behind.

Both hip fracture and coxarthrosis patients exhibited comparable bone tissue composition. That is in contrast to other studies that demonstrated significant variations in matrix maturity (amide I subpeak intensities ratio I_{1660}/I_{1690}) [83,84] or mineralized collagen fibril alignment (I_{1044}/I_{956} and I_{1244}/I_{1268}) [82]. However, the measured sample volume in the present study was far (often in the opposite quadrant) from the fracture site. A stronger correlation between the tissue composition and the fracture occurrence is anticipated for the fractured regions.

In the current work, only bone compositional characteristics were found to correlate with the patient's age, similar to other studies mentioned in Table 3. In particular, the bone mineral to matrix ratio decreased with age while amide I sub-peak ratio $I_{\sim1660}/I_{\sim1683}$ is increasing. The former might be an unexpected finding because it is well-accepted that mineralization generally increases with age [85] or stays constant after reaching skeletal maturity [67]. The majority of previous studies on bone compositional assessment in humans did not find a significant correlation between various mineral to matrix ratios and the patient's age (Table 3). In the present work, the mineral to matrix ratio was measured as an integrated area ratio of secondary phosphate over amide III. This ratio was not reported in earlier studies on aging human bones. However, it should be included in the future since it is independent of the incoming laser polarization and correlates with the Ca content [43]. The observed decrease in the mineral to matrix ratio in the current study is likely due to the organic contribution (amide III).

Furthermore, we observe an increase with age amide I sub-peak ratio $I_{\sim1660}/I_{\sim1683}$. Similarly, the amide I area [86] as well as the amide I sub-peak ratio $I_{\sim1660}/I_{\sim1690}$ was shown to positively correlate with age [47] (Table 3), yet the physical origin of these sub-peaks is not well understood. Some studies claim that this sub-peak ratio corresponds to the one collected through FTIR, where it provides the ratio of non-reducible (mature trivalent) over reducible (immature divalent) enzymatic crosslinks [87]. However, it is debatable whether this sub-peak ratio can represent mature to immature crosslink ratio in Raman spectroscopy measurements [49]. In FTIR studies, this crosslink ratio increased with osteoporosis [83] and fractures [84].

Although the observed dependence of the Raman ratios from age is significant ($p \leq 0.04$), the coefficient of determination is quite low for both mineral to matrix ratio and the amide I sub-peak ratio ($R^2 \leq 0.13$). The fact that there is a significant correlation might come from the high number of samples.

We hypothesize that the observed interplay of the mineral-organic fractions may smoothen the observed variations in the mechanical properties versus the patients' age. As a potential pathway, extensive collagen cross-linking may increase the stiffness of the organic part, thus compensating for the reduced tissue mineralization and keeping the averaged microscale mechanical properties constant for patients at ages 45 to 89. Similar conclusions were drawn in the work of Fratzl-Zelman et al.[62].

4.3. Site-matched analysis of the bone structure-property relationship

Besides assessing averaged microscale properties of the compact bone, site-matched qPRS with nanoindentation, as well as micropillar compression, allowed assessing local structure-property relationship analysis. All investigated mechanical properties except yield strain demonstrate a weak ($R^2 < 0.15$) but significant ($p < 0.05$) positive correlation with the mineral fraction of bone, which is in line with previous studies [70,93,94]. On the averaged bone level, the correlation between the yield stress, elastic moduli and hardness versus TMD (Fig. 7, Pearson's coefficients 0.4, 0.3 and 0.4 accordingly) was comparable to the one at the local site-matched analyses. Interestingly, the highest correlations for the site-matched local analysis were observed between the yield stress vs. the mineral to matrix ratio and the elastic modulus vs. the mineral crystallinity (Fig. 7, Pearson's coefficients 0.4 for both). This suggests that the yield properties of bone lamellae depend on both mineral and organic bone portions, while elastic properties are more strongly influenced by changes in the mineral bone phase. However, as discussed in Section 4.2, it is actually the interplay of organic and mineral phases that affects the mechanical properties [95,96].

To our surprise, local micromechanical properties were independent of the out-of-plane MCF angle. The inclusion of the angle in a multilinear model for the local mechanical properties versus the mineral to matrix ratio did not improve the correlation. This is striking since a strong dependence on the out-of-plane MCF angle is expected for this anisotropic nanocomposite and was demonstrated in earlier studies [35]. A likely explanation for this discrepancy is the diverging volume of interest of the different measurements. For the nanoindentation maps, qPRS measurements were carried inside the map, yet not within exact indentation spots but rather in between. Since the distance between the indents was 20 μm, different lamellae could have been measured. While the polarized Raman spectra from the bone micropillar were collected within the pillar dimensions, the analyzed volumes from qPRS (~8.6 μm^3) and compressions (~90 μm^3) were around an order of magnitude different. Thus, the MCF orientation within the larger portion of the micropillar volume was not analyzed. In future studies, care should be taken to strictly site-match measurements and to choose volumes of interest for the microstructural measurements as close as possible to those of the mechanical measurements. Yet the microscale mechanical properties demonstrate a prominent correlation with the mineral to matrix ratio, suggesting that the local composition is more continuous at measured volumes.

Table 3
Overview of other works where bone compositional properties in relation to patient age and/or fracture occurrence were assessed via vibrational spectroscopy (Raman, FTIR).

Samples	Method	Mineral to matrix ratio	Collagen dis./order ratio	Collagen maturity ratio	Crystallinity	Ref
Proximal femur cortical bone (N = 39, 46–99 years)	Raman, 633 nm	$A_{\nu_1PO_4}/A_{amide\ I}$ NS with age	–	–	$1/FWHM(\nu_1PO_4)$ NS with age	[67]
Proximal femur cortical bone (N = 58, 21–101 years)	Raman, 785 nm	$A_{\nu_1PO_4}/A_{amide\ I}$ NS with age $A_{\nu_1PO_4}/A_{amide\ III}$ ↑ with age for male donors	I_{1670}/I_{1640} (*amide I sub bands*) ↑ with age	I_{1670}/I_{1690} (*amide I sub bands*) ↑ with age	–	[47]
Mid-diaphyseal femur, cortical bone (N = 16, 52–85 years)	Raman, 633 nm	I_{960}/I_{1450} (ν_1PO_4/CH_2) ↑ with age	–	–	$1/FWHM(\nu_1PO_4)$ NS with age	[88]
Femur cortical bone (N = 62, 21–101 years)	Raman, 785 nm	$I_{\nu_1PO_4}/I_{amide\ III}$ NS with age	–	–	$1/FWHM(\nu_1PO_4)$ NS with age	[89]
Femoral neck cortical bone (N = 42, 45–89 years); fracture (N = 11) and coxarthrosis (N = 31)	Raman, 633 nm	$A_{\nu_2PO_4}/A_{amide\ III}$ ↓ with age, NS between fract./coxarth.	$I_{\sim1670}/I_{\sim1640}$ (*amide I sub bands*) NS with age, NS between fract./coxart.	$I_{\sim1660}/I_{\sim1683}$ (*amide I sub bands*) ↑ with age, NS between fract./coxarth	$1/FWHM(\nu_1PO_4)$ NS with age, NS between fract./coxart.	Pres. work
Femoral head (N = 26, 50–72 years, women); fracture (N = 15) and controls (N = 11)	Raman, 785 nm	$A_{\nu_1PO_4}/A_{amide\ I}$ NS between fract./non-fract.	–	–	–	[90]
Mid-diaphyseal humerus cortical bone (N = 9, 34–99 years)	Raman, 244 nm	–	–	$A_{amide\ I}$ ↑ with age	–	[86]
Transiliac bone trabeculae (N = 54, 1.5–23 years)	Raman, 785 nm	$A_{\nu_1PO_4}/A_{amide\ III}$ NS with age	–	$I_{1660}/A_{amide\ I\ (1620–1700)}$ NS with age	$1/FWHM(\nu_1PO_4)$ NS with age	[91]
Iliac cortical bone (N = 21, 10–12 years), juvenile osteoporosis (N = 9) vs controls (N = 12)	FTIR	$A_{\nu_1PO_4}/A_{amide\ I}$ NS between groups	–	I_{1660}/I_{1690} ↑ in juvenile osteoporosis patients	I_{1030}/I_{1020} NS between groups	[83]
Iliac bone from women with fracture (N = 60) and without (N = 60)	FTIR	$A_{\nu_1PO_4}/A_{amide\ I}$ NS between groups	–	I_{1660}/I_{1690} NS btw groups	I_{1030}/I_{1020} NS between groups	[92]
Iliac bone from women with fracture (N = 32) and without (N = 22)	FTIR	$A_{\nu_1PO_4}/A_{amide\ I}$ NS between groups	–	I_{1660}/I_{1690} ↑ in fractured patients	I_{1030}/I_{1020} NS between groups	[84]

A = peak area, I = peak intensity, NS = non-significant.

4.4. Potential markers of bone quality

This study provides a framework of laboratory-based methods for the bone composition, morphology, elastic and yield mechanical properties analysis. Consequently, wide spectra of bone parameters were measured and correlated with the patient's sex, primary diagnosis and age. Another motivation for this study was to find the most prospective bone characteristics which could be used for fracture risk prediction in the future. For this, we run a Gaussian Naïve Bayes classification algorithm on the final matrix of collected bone properties per patient. Naïve Bayes is a common method for building prediction models for a binary outcome and has been extended for disease classification [57–59], including osteoporosis [60]. Here, we apply this algorithm to multimodal characteristics of bone for fracture prediction.

Naïve Bayes classification algorithm was trained on the dataset from 32 patients and reached the 0.7 prediction accuracy during the test phase on the remaining patients dataset, meaning that 7 out of ten patients were correctly classified (Fig. B3). Yet, from the confusion matrix, it seems that the algorithm will likely identify a true fracture patient as it would assign it to the coxarthrosis cohort. But because the number of tests is so low, an additional characteristic is involved for the model accuracy estimation – the Area Under the Curve (AUC) of the Receiver Operating Characteristic (ROC), which evaluates the classifier performance over all possible sensitivity thresholds. As a result, 0.71 AUC score was achieved, highlighting the perspective variables for bone fracture prediction: the mineral to matrix ratio, indentation hardness and micropillar yield stress. All of these are often overlooked and are not included in general patient screening due to the lack of high-precision, low-cost instruments for their measurements.

Nowadays, more and more studies emphasize the influence of micromechanical bone properties on macroscale bone strength and toughness [67]. We can only anticipate the future bone characterization techniques and their potential impact. Moreover, bone compositional properties, as assessed via Raman spectroscopy, were also shown to correlate with bone fracture toughness [46,47]. This is in line with the proposed classification model, where mineral to matrix ratio demonstrates a strong influence on fracture prediction. Surprisingly, patient age did not dominate the fracture prediction model. However, the influence of age might be indirectly included in the model through compositional variations (e.g. mineral to matrix ratio, matrix maturity ratio). From the patient cohort analysis, it is evident that older patients have an increased risk of bone fractures, in line with the clinical fracture risk questionnaire.

It is important to highlight that the sample size in this analysis is too low to claim a universal classification model. With the small to moderate sample size and unbalanced dataset, the Naïve Bayes is prone to prediction bias. However, the proposed analysis strategy can be applied in further research on combining different bone quantity and quality parameters for fracture risk predictions. Although challenging to achieve in a laboratory setting, a larger number of patients ($N > 200$) is required.

4.5. General limitations

In the present study, cortical bone properties of hip fracture patients were compared to the ones of coxarthrosis patients. Although coxarthrosis patients cannot be assigned to a control group, we do not expect an influence of the osteoarthritis on the femoral neck cortical bone properties. While a large influence is observed in the subchondral bone region due to the bone-to-bone contact, this is usually limited to the millimeter range from the subchondral bone surface and it is debatable whether coxarthrosis may affect cortical bone at the femoral neck [97,98]. However, severe coxarthrosis may alter the gait, consequently affecting the stress distribution in the femoral neck, bone remodeling and, thus, bone ECM properties [99]. In the current study, no patient information about the severity of coxarthrosis or gait alteration was available.

Collected clinical information from the patients involved in this study was fairly limited and did not include BMD values for osteoporosis and/or osteopenia screening. However, previous bone fractures for the population >50 y.o. is considered one of the major risk factors for osteoporosis [100]. Therefore, in this study, we consider the cohort of patients with fractures as patients at a high risk of osteoporosis. In addition, no clinical record of long-term medication was available. Bisphosphonate drugs have a drastic influence on bone remodeling and mineralization levels [101] and would certainly have affected the observed variations in the measured bone properties.

As anticipated, femoral neck height and morphologies were not always consistent between the patients. Nevertheless, the surgeon followed the double osteotomy protocol, aiming to extract approximately 10 mm femoral neck slices from all patients. Originally 59 femoral necks were extracted during the surgeries and further screened using the laboratory-based micro-CT. In the end, only 42 femoral necks had intact inferomedial regions and were used in this study. Inconsistent morphology between the samples restricted comparative morphological analysis. For future study planning, it is crucial to take into account the morphological variations between the human bone samples, leading to decreased number of suitable biopsies.

As discussed above, all reported measurements in this study were carried out on the inferomedial part of the femoral neck slice. This region carries most of the compressive loading in the femoral neck site [102,103] and consequently has an abundant amount of cortical bone, sufficient for the micropillar fabrication. At the same time, hip fractures were mainly located in the supero-posterior and -anterior quadrants of the excised femoral neck sections, almost opposite to the measured inferomedial region. Thus, the sampling location might have diminished any potential differences between the fractured and non-fractured cohorts. While it would be challenging to perform the micropillar compression experiments, nanoindentation and polarized Raman spectroscopy could potentially be applied in the future studies in the fractured hip regions. However, several limitations have to be overcome first. For example, (1) scaling down the analysis to match the lower amount of cortex, and (2) increasing the number of patients since this neck region is often fragmented and poorly suitable for the analysis proposed in this study.

We would like to highlight that all the samples used in the study were fixed and embedded due to biosafety regulations in the testing facilities. This procedure, in principle, affects the organic fraction of the bone matrix [81] and slightly modifies the mechanical properties of the bone: an increase in stiffness and compressive strength is reported [104,105]. While bone tissues with different mineralization may be altered to varying degrees by fixation with ethanol, we observe small variations in TMD between the samples and therefore do not account for possible

discrepancies. Moreover, all specimens were fixed the same way, allowing a relative comparison between samples. For future studies involving compositional analysis, the use of fresh bone samples is endorsed. With this respect, the use of the outlined laser ablation protocol will be invaluable since it allows preparing the microscale samples avoiding any vacuum conditions.

Finally, yet importantly, there is always room for more study participants and additional clinical information. A simplified statistical power analysis has been performed with respect to discrete and continuous variables [106]. For the available sample size (N = 42), with an α error probability of 0.05, an allocation ratio of 3, and the effect of size d = 0.80, differences in the mean of 10 % can be detected with a power of 0.8 [106]. A further power analysis for multiple linear regressions with an α error probability of 0.05 and 2 predictor variables showed that relatively weak trends with partial R^2 of 0.20 can be detected with a power of 0.8. [106]. To reach the detection power of 0.95 for both discrete and continuous variables, in future studies with a similar sample number and allocation ratio, a minimum of 70 patients is required. Moreover, having patients screened for osteoporosis or osteopenia would have as well improved the final analysis of the potential bone quality markers. Although we consider the hip fracture patient as being at high risk of osteoporosis, additional clinical screening is mandatory before assigning them to osteoporotic cases.

5. Conclusion

In this study, bone quality and quantity were assessed at the femoral neck sites of the patients who underwent hip arthroplasty. For the first time the microscale yield properties of the human cortical bone were assessed in a large number of patients (N = 42). A combination of high-throughput micromechanical testing techniques (nanoindentation, micropillar compression) together with micro-CT and quantitative polarized Raman spectroscopy allowed us to create a comprehensive data frame of the bone properties for each patient. Microscale mechanical and morphological properties at the compact bone level were independent of patient age, sex or fracture occurrence. Only local bone composition (specifically mineral to matrix ratio and $I_{\sim1660}/I_{\sim1683}$ ratio), as assessed via qPRS, showed weak but significant correlation with age. The site-matched analysis of microscale mechanical, compositional and morphological properties allowed for quantifying compact bone's local structure-properties relationships. Microscale yield stress, elastic modulus and hardness demonstrate a positive correlation with the mineral fraction of bone, but no correlation with the out-of-plane angle of the mineralized collagen fibrils. With Naïve Bayes algorithms, a classification model was built for hip fracture prediction at a 0.7 accuracy. Accordingly, the mineral to matrix ratio, indentation hardness and micropillar yield stress are the most prospective parameters for fracture risk prediction in laboratory settings. The presented data and methodological framework can be used in the future studies on comparing laboratory and clinical methods for the prediction of fracture risk. However, such studies require a much larger number of patients (N > 200).

CRediT authorship contribution statement

Tatiana Kochetkova: Writing – review & editing, Writing – original draft, Visualization, Validation, Software, Project administration, Methodology, Investigation, Formal analysis, Data curation, Conceptualization. **Markus S. Hanke:** Writing – review & editing, Resources, Project administration, Methodology, Investigation, Conceptualization. **Michael Indermaur:** Writing – review & editing, Investigation, Formal analysis, Data curation. **Alexander Groetsch:** Writing – review & editing, Methodology, Investigation. **Stefan Remund:** Writing – review & editing, Methodology. **Beat Neuenschwander:** Writing – review & editing, Resources, Methodology. **Johann Michler:** Writing – review & editing, Resources, Funding acquisition. **Klaus A. Siebenrock:** Writing – review & editing, Resources, Funding acquisition. **Philippe Zysset:** Writing – review & editing, Supervision, Resources, Conceptualization. **Jakob Schwiedrzik:** Writing – review & editing, Supervision, Resources, Funding acquisition, Conceptualization.

Declaration of competing interest

The authors declare that they have no known competing financial interests or personal relationships that could have appeared to influence the work reported in this paper.

Data availability

The collected data and processing scripts from this study are available upon request.

Acknowledgments

This work is funded by the Special Focus Area Personalized Health and Related Technologies (SFA PHRT) iDoc Project 2017-304. The authors would like to thank B. Voumard, E. Jäggi and K. Leeb for the sample and patient information collection; K. Lang, S. Owusu and D. Bosshardt for their support during bone sample fixation. F. Klimashin for the assistance with the nanoindentation setup, C. Peruzzi and D. Casari for the FE simulations. F. Kurdzesau, P. Bühlmann for their statistical advice and G. Goyal for her great help with the PCA and classification algorithms. The authors would like to acknowledge the valuable scientific suggestions of Prof. J. Nyman.

Appendix A. Micro-CT data processing

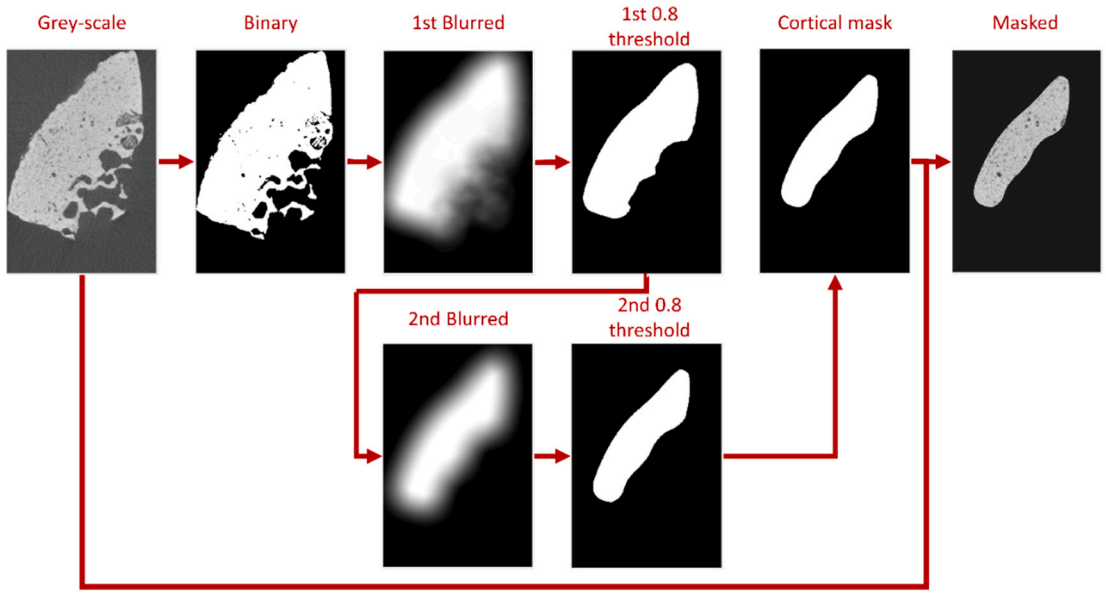

Fig. A1. Steps of the micro-CT image processing.

Appendix B. Principal Component Analysis (PCA) and hip fracture prediction (classification) on the final dataset

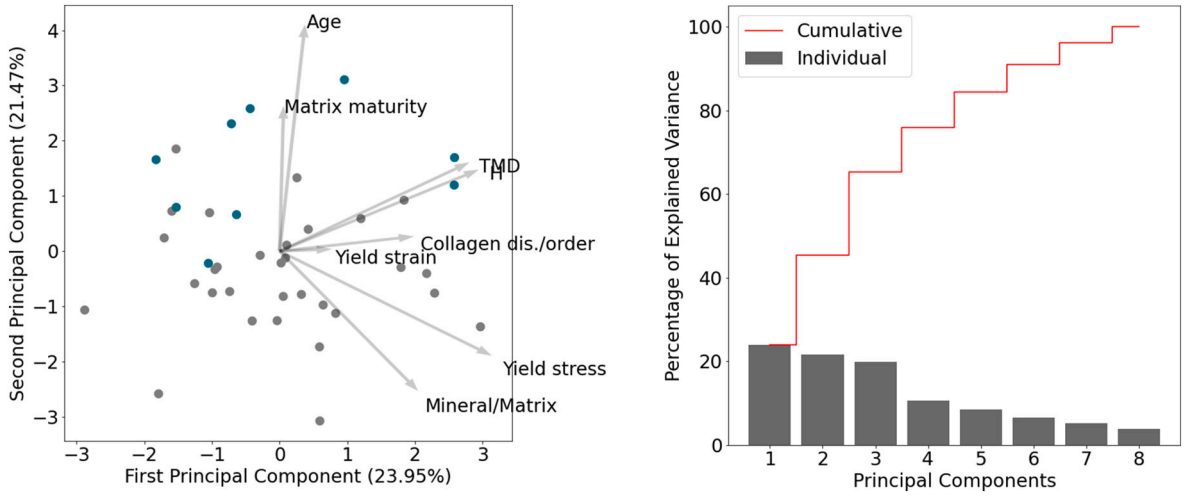

Fig. B1. Principal component analysis outputs. Left: PCA analysis with first two principal components (PC) score distributions for all 42 patients, with the loading plots atop the PCA, showing how strongly each variable influences the first two PC; colors of the points correspond to the patients' primary diagnoses: coxarthrosis – grey, fracture – aquamarine. Right: Explained variance from each of the PC. Note that 95 % of the variation is explained by the first 7 PC.

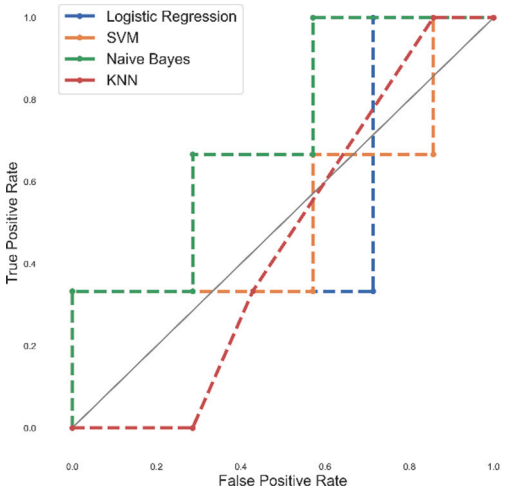

Classification algorithm	Accuracy	AUC
Logistic Regression	0.7	0.52
SVM	0.7	0.52
Naïve Bayes	**0.7**	**0.71**
KNN	0.5	0.45

Fig. B2. Assessing the classification algorithms performance. Left: Receiver Operating Characteristic (ROC) curve for four classification algorithms (logistic regression, support vector machines (SVM), Naïve Bayes and K nearest neighbor (KNN)). Right: Classification algorithms accuracy and area under the ROC curve (AUC) characteristics.

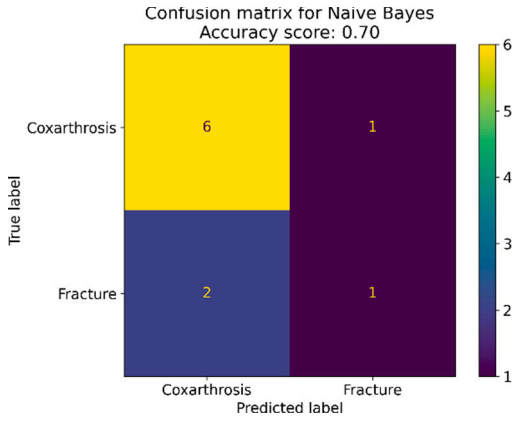

Feature	Abs contribution to the model
Mineral/Matrix ratio	**0.16**
Yield stress	**0.06**
H	**0.06**
Amide I sub-peak ratio $I_{\sim 1670}/I_{\sim 1640}$	0.04
Amide I sub-peak ratio $I_{\sim 1660}/I_{\sim 1683}$	0.04
Age	0.02
Yield strain	0.02
TMD	0.01

Fig. B3. Prediction of the bone fracture patients via Naïve Bayes algorithm. Left: Confusion matrix for the classification. Right: Dataset variables (features) sorted per importance.

References

[1] F. Borgström, L. Karlsson, G. Ortsäter, N. Norton, P. Halbout, C. Cooper, M. Lorentzon, E.V. McCloskey, N.C. Harvey, M.K. Javaid, J.A. Kanis, J. Y. Reginster, S. Ferrari, Arch. Osteoporos. 15 (2020).
[2] G.S. Keene, M.J. Parker, G.A. Pryor, Br. Med. J. 307 (1993) 1248–1260.
[3] K. Hertz, Santy-Tomlinson, Fragility Fracture Nursing Holistic Care and Management of the Orthogeriatric Patient Perspectives in Nursing Management and Care for Older Adults Series Editors, 2018.
[4] S.C.E. Schuit, M. Van Der Klift, A.E.A.M. Weel, C.E.D.H. De Laet, H. Burger, E. Seeman, A. Hofman, A.G. Uitterlinden, J.P.T.M. Van Leeuwen, H.A.P. Pols, Bone 34 (2004) 195–202.
[5] J.A. Gasser, M. Kneissel, in: S.Y. Smith, A. Varela, R. Samadfam (Eds.), Bone Toxicology, Springer International Publishing, Cham, 2017, pp. 27–94.
[6] O. Johnell, J.A. Kanis, Osteoporos. Int. 17 (2006) 1726–1733.
[7] P. Barry, T. Aspray, K. Briers, G. Collins, J. Compston, F. Dockery, S. Ruddick, P. Selby, D. Stephens, A. Thornhill, J. Tobias, National Institute for Health and Clinical Excellence, 2012, pp. 1–97.
[8] G.N. Grob, Aging Bones: A Short History of Osteoporosis, Johns Hopkins University Press, Baltimore, 2014.
[9] J.T. Lin, J.M. Lane, Clin. Orthop. Relat. Res. 425 (2004) 126–134.
[10] R.S. Stafford, R.L. Drieling, A.L. Hersh, Arch. Intern. Med. 164 (2004) 1525.
[11] D.M. Black, J.A. Cauley, R. Wagman, K. Ensrud, H.A. Fink, T.A. Hillier, L.-Y. Lui, S.R. Cummings, J.T. Schousboe, N. Napoli, J. Bone Miner. Res. 33 (2018) 389–395.
[12] D.G. Hansen, T. Tutaworn, J.M. Lane, J. Bone Joint Surg. 104 (2022) 1509–1515.
[13] A. Marques, R.J.O.O. Ferreira, E. Santos, E. Loza, L. Carmona, J.A.P. Da Silva, Ann. Rheum. Dis. 74 (2015) 1958–1967.
[14] C. Greenwood, J. Clement, A. Dicken, J.P.O.O. Evans, I. Lyburn, R.M. Martin, K. Rogers, N. Stone, P. Zioupos, Bone 93 (2016) 55–63.
[15] E. Donnelly, Clin. Orthop. Relat. Res. 469 (2011) 2128–2138.
[16] P. Ammann, A.R. Rizzoli, R. Rizzoli, Osteoporos. Int. 14 (Suppl. 3) (2003) 13–18.
[17] H. Sievänen, P. Kannus, T.L.N. Järvinen, PLoS Med. 4 (2007), e27.
[18] R.R. Recker, M. Janet Barger-Lux. https://www.scopus.com/record/display.uri?eid=2-s2.0-17144419988&origin=resultslist&sort=plf-f&src=s&sid=9ecfb75a22758f9e5a59d7505f657044&sot=b&sdt=b&s=DOI%2810.1007%2Fs11914-004-0017-z%29&sl=46&sessionSearchId=9ecfb75a22758f9e5a59d7505f657044, 2004.
[19] J. Compston, Arq. Bras. Endocrinol. Metabol. 50 (2006) 579–585.
[20] D.P. Fyhrie, J. Musculoskelet. Neuronal Interact. 5 (2005) 318–320.
[21] E.A. Taylor, E. Donnelly, Bone 139 (2020).
[22] M. Georgiadis, R. Müller, P. Schneider, J. R. Soc. Interface 13 (2016).
[23] R.O. Ritchie, K.J. Koester, S. Ionova, W. Yao, N.E. Lane, J.W. Ager, Bone 43 (2008) 798–812.
[24] J.S. Nyman, A.J. Makowski, Curr. Osteoporos. Rep. 10 (2012) 169–177.
[25] A.H. Burstein, J.M. Zika, K.G. Heiple, L. Klein, J. Bone Joint Surg. Am. 57 (1975) 956–961.
[26] J.D. Currey, J. Biomech. 21 (1988) 131–139.
[27] J.S. Nyman, A. Roy, R.L. Acuna, H.J. Gayle, M.J. Reyes, J.H. Tyler, D.D. Dean, X. Wang, Bone 39 (2006) 1210–1217.
[28] J.S. Nyman, A. Roy, X. Shen, R.L. Acuna, J.H. Tyler, X. Wang, J. Biomech. 39 (2006) 931–938.
[29] S. Weiner, H.D. Wagner, Annu. Rev. Mater. Sci. 28 (1998) 271–298.
[30] P. Fratzl, R. Weinkamer, Prog. Mater. Sci. 52 (2007) 1263–1334.
[31] J. Schwiedrzik, R. Raghavan, A. Bürki, V. Lenader, U. Wolfram, J. Michler, P. Zysset, Nat. Mater. 13 (2014) 740–747.
[32] W.C.C. Oliver, G.M.M. Pharr, J. Mater. Res. 7 (1992) 1564–1583.
[33] T. Kochetkova, A. Groetsch, M. Indermaur, C. Peruzzi, S. Remund, B. Neuenschwander, B. Bellon, J. Michler, P. Zysset, J. Schwiedrzik, J. Mech. Behav. Biomed. Mater. 134 (2022) 105405.
[34] L. Bozec, M. Odlyha, Biophys. J. 101 (2011) 228–236.

[35] T. Kochetkova, C. Peruzzi, O. Braun, J. Overbeck, A.K. Maurya, A. Neels, M. Calame, J. Michler, P. Zysset, J. Schwiedrzik, Acta Biomater. 119 (2021) 390–404.
[36] C. Peruzzi, R. Ramachandramoorthy, A. Groetsch, D. Casari, P. Grönquist, M. Rüggeberg, J. Michler, J. Schwiedrzik, Acta Biomater. 131 (2021) 403–414.
[37] G. Van Rossum, F.L. Drake, Python 3 Reference Manual, CreateSpace, Scotts Valley, CA, 2009.
[38] A. Groetsch, S. Stelzl, Y. Nagel, T. Kochetkova, N.C. Scherrer, A. Ovsianikov, J. Michler, L. Pethö, G. Siqueira, G. Nyström, J. Schwiedrzik, Small 19 (2023).
[39] H. Zhang, B.E. Schuster, Q. Wei, K.T. Ramesh, Scr. Mater. 54 (2006) 181–186.
[40] M. Smith, ABAQUS/Standard User's Manual, Version 6.9, Dassault Systèmes Simulia Corp, Providence, RI, 2009.
[41] M. Müller, Introduction to Confocal and Fluorescence Microscopy, Second ed., SPIE, Bellingham, WA, 2006.
[42] M.K. Nieuwoudt, R. Shahlori, D. Naot, R. Patel, H. Holtkamp, C. Aguergaray, M. Watson, D. Musson, C. Brown, N. Dalbeth, J. Cornish, M.C. Simpson, Sci. Rep. 10 (2020).
[43] A. Roschger, S. Gamsjaeger, B. Hofstetter, A. Masic, S. Blouin, P. Messmer, A. Berzlanovich, E.P. Paschalis, P. Roschger, K. Klaushofer, P. Fratzl, J. Biomed. Opt. 19 (2014) 65002.
[44] D.F. Ge, C. Rey, P.D. Delmas, G. Boivin, 433–445, https://www.scopus.com/record/display.uri?eid=2-s2.0-77956471741&origin=resultslist&sort=plf-f&src=s&sid=9ecfb75a22758f9e5a59d7505f657044&sot=b&sdt=b&s=DOI%2810.1007%2Fs00774-009-0146-7%29&sl=30&sessionSearchId=9ecfb75a22758f9e5a59d7505f657044, 2010.
[45] M.D. Morris, G.S. Mandair, Clin. Orthop. Relat. Res. 469 (2011) 2160–2169.
[46] M. Unal, H. Jung, O. Akkus, J. Bone Miner. Res. 31 (2016) 1015–1025.
[47] M. Unal, S. Uppuganti, S. Timur, A. Mahadevan-Jansen, O. Akkus, J.S. Nyman, Sci. Rep. 9 (2019) 1–13.
[48] E.M.B. McNerny, B. Gong, M.D. Morris, D.H. Kohn, J. Bone Miner. Res. 30 (2015) 446–455.
[49] M. Unal, R. Ahmed, A. Mahadevan-Jansen, J.S. Nyman, Analyst 146 (2021) 7444.
[50] R Core Team. https://www.R-project.org/, 2021.
[51] A. Kassambara. https://CRAN.R-project.org/package=rstatix, 2021.
[52] D. Bates, M. Mächler, B. Bolker, S. Walker, J. Stat. Softw. 67 (2015).
[53] C.R. Harris, K.J. Millman, S.J. van der Walt, R. Gommers, P. Virtanen, D. Cournapeau, E. Wieser, J. Taylor, S. Berg, N.J. Smith, R. Kern, M. Picus, S. Hoyer, M.H. van Kerkwijk, M. Brett, A. Haldane, J.F. del Río, M. Wiebe, P. Peterson, P. Gérard-Marchant, K. Sheppard, T. Reddy, W. Weckesser, H. Abbasi, C. Gohlke, T.E. Oliphant, Nature 585 (2020) 357–362.
[54] F. Pedregosa, G. Varoquaux, A. Gramfort, V. Michel, B. Thirion, O. Grisel, M. Blondel, A. Müller, J. Nothman, G. Louppe, P. Prettenhofer, R. Weiss, V. Dubourg, J. Vanderplas, A. Passos, D.É. Duchesnay, J. Mach. Learn. Res. 12 (2011) 2825–2830.
[55] M. Langarizadeh, F. Moghbeli, Acta Inform. Med. 24 (2016) 364–369.
[56] P.K. Zysset, Osteoporos. Int. 20 (2009) 1049–1055.
[57] I. Kononenko, Machine Learning for Medical Diagnosis: History, State of the Art and Perspective. https://www.scopus.com/record/display.uri?eid=2-s2.0-0034922742&origin=resultslist&sort=plf-f&src=s&sid=9ecfb75a22758f9e5a59d7505f657044&sot=b&sdt=b&s=DOI%2810.1016%2FS0933-3657%2801%2900077-X%29&sl=30&sessionSearchId=9ecfb75a22758f9e5a59d7505f657044.
[58] A. Awaysheh, J. Wilcke, F. Elvinger, L. Rees, W. Fan, K.L. Zimmerman, Vet. Pathol. 56 (2019) 512–525.
[59] M. Shehab, L. Abualigah, Q. Shambour, M.A. Abu-Hashem, M.K.Y. Shambour, A. I. Alsalibi, A.H. Gandomi, Comput. Biol. Med. 145 (2022).
[60] C. bin Huang, J. sen Hu, K. Tan, W. Zhang, T. hao Xu, L. Yang, BMC Geriatr. 22 (2022).
[61] P.K. Zysset, X. Edward Guo, C. Edward Hoffler, K.E. Moore, S.A. Goldstein, J. Biomech. 32 (1999) 1005–1012.
[62] N. Fratzl-Zelman, P. Roschger, A. Gourrier, M. Weber, B.M. Misof, N. Loveridge, J. Reeve, K. Klaushofer, P. Fratzl, Calcif. Tissue Int. 85 (2009) 335–343.
[63] A.G. Reisinger, D.H. Pahr, P.K. Zysset, J. Mech. Behav. Biomed. Mater. 4 (2011) 2113–2127.
[64] G. Franzoso, P.K. Zysset, J. Biomech. Eng. 131 (2009) 1–11.
[65] P. Milovanovic, J. Potocnik, D. Djonic, S. Nikolic, V. Zivkovic, M. Djuric, Z. Rakocevic, Exp. Gerontol. 47 (2012) 154–159.
[66] J.Y. Rho, P. Zioupos, J.D. Currey, G.M. Pharr, J. Biomech. 35 (2002) 189–198.
[67] M.J. Mirzaali, J.J. Schwiedrzik, S. Thaiwichai, J.P. Best, J. Michler, P.K. Zysset, U. Wolfram, Bone 93 (2016) 196–211.
[68] T. Jenkins, O.L. Katsamenis, O.G. Andriotis, L.V. Coutts, B. Carter, D.G. Dunlop, R.O.C. Oreffo, C. Cooper, N.C. Harvey, P.J. Thurner, the OStEO group, J. Mech. Behav. Biomed. Mater. 75 (2017) 399–412.
[69] A. Bonicelli, T. Tay, J.P. Cobb, O.R. Boughton, U. Hansen, R.L. Abel, P. Zioupos, J. Mech. Behav. Biomed. Mater. 138 (2023) 105573.
[70] M. Indermaur, D. Casari, T. Kochetkova, C. Peruzzi, E. Zimmermann, F. Rauch, B. Willie, J. Michler, J. Schwiedrzik, P. Zysset, J. Bone Miner. Res. 00 (2021) 1–12.
[71] O.A. Tertuliano, J.R. Greer, Nat. Mater. 15 (2016) 1195–1202.
[72] A. Groetsch, A. Gourrier, J. Schwiedrzik, M. Sztucki, R.J. Beck, J.D. Shephard, J. Michler, P.K. Zysset, U. Wolfram, Acta Biomater. 89 (2019) 313–329.
[73] J. Schwiedrzik, A. Taylor, D. Casari, U. Wolfram, P. Zysset, J. Michler, Acta Biomater. 60 (2017) 302–314.
[74] T. Yamamoto, K. Uchida, K. Naruse, M. Suto, K. Urabe, K. Uchiyama, K. Suto, M. Moriya, M. Itoman, M. Takaso, Cell Tissue Bank. 13 (2012) 409–414.
[75] D. Casari, J. Michler, P. Zysset, J. Schwiedrzik, Acta Biomater. 120 (2020) 135–145.
[76] B. Voumard, P. Stefanek, M. Pretterklieber, D. Pahr, P. Zysset, Bone Rep. 17 (2022) 101638.
[77] V. Sansalone, V. Bousson, S. Naili, C. Bergot, F. Peyrin, J.D. Laredo, G. Haïat, Bone 50 (2012) 876–884.
[78] K.E.S. Poole, G.M. Treece, P.M. Mayhew, J. Vaculík, P. Dungl, M. Horák, J. J. Štěpán, A.H. Gee, PLoS One 7 (2012).
[79] J.S. Yerramshetty, O. Akkus, Bone 42 (2008) 476–482.
[80] J.S. Nyman, A.J. Makowski, C.A. Patil, T.P. Masui, E.C. O'Quinn, X. Bi, S. A. Guelcher, D.P. Nicollela, A. Mahadevan-Jansen, E.C. O'Quinn, X. Bi, S. A. Guelcher, D.P. Nicollela, A. Mahadevan-Jansen, Calcif. Tissue Int. 89 (2011) 111–122.
[81] Y.N. Yeni, J. Yerramshetty, O. Akkus, C. Pechey, C.M. Les, Calcif. Tissue Int. 78 (2006) 363–371.
[82] G.S. Mandair, M.P. Akhter, F.W.L.L. Esmonde-White, J.M. Lappe, S.P. Bare, W. R. Lloyd, J.P. Long, J. Lopez, K.M. Kozloff, R.R. Recker, M.D. Morris, Bone 148 (2021) 115962.
[83] I. Garcia, V. Chiodo, Y. Ma, A. Boskey, Connect. Tissue Res. 57 (2016) 28–37.
[84] S. Gourion-Arsiquaud, D. Faibish, E. Myers, L. Spevak, J. Compston, A. Hodsman, E. Shane, R.R. Recker, E.R. Boskey, A.L. Boskey, J. Bone Miner. Res. 24 (2009) 1565–1571.
[85] O. Akkus, F. Adar, M.B. Schaffler, Bone 34 (2004) 443–453.
[86] J.W. Ager, R.K. Nalla, K.L. Breeden, R.O. Ritchie, J. Biomed. Opt. 10 (2005), 034012.
[87] E.P. Paschalis, K. Verdelis, S.B. Doty, A.L. Boskey, R. Mendelsohn, M. Yamauchi, J. Bone Miner. Res. 16 (2001) 1821–1828.
[88] J.S. Yerramshetty, C. Lind, O. Akkus, Bone 39 (2006) 1236–1243.
[89] A.J. Makowski, M. Granke, S. Uppuganti, A. Mahadevan-Jansen, J.S. Nyman, p. 930341, https://www.scopus.com/record/display.uri?eid=2-s2.0-84926638071&origin=resultslist&sort=plf-f&src=s&sid=9ecfb75a22758f9e5a59d7505f657044&sot=b&sdt=b&s=DOI%2810.1117%2F12.2080350%29&sl=34&sessionSearchId=9ecfb75a22758f9e5a59d7505f657044, 2015.
[90] B.R. McCreadie, M.D. Morris, T. ching Chen, D. Sudhaker Rao, W.F. Finney, E. Widjaja, S.A. Goldstein, Bone 39 (2006) 1190–1195.
[91] S. Gamsjaeger, B. Hofstetter, N. Fratzl-Zelman, P. Roschger, A. Roschger, P. Fratzl, W. Brozek, A. Masic, B.M. Misof, F.H. Glorieux, K. Klaushofer, F. Rauch, E.P. Paschalis, Bone 69 (2014) 89–97.
[92] A.L. Boskey, E. Donnelly, E. Boskey, L. Spevak, Y. Ma, W. Zhang, J. Lappe, R. R. Recker, J. Bone Miner. Res. 31 (2016) 1070–1081.
[93] M. Unal, A. Creecy, J.S. Nyman, Curr. Osteoporos. Rep. 16 (2018) 205–215.
[94] H. Follet, G. Boivin, C. Rumelhart, P.J. Meunier, Bone 34 (2004) 783–789.
[95] H.S. Gupta, J. Seto, W. Wagermaier, P. Zaslansky, P. Boesecke, P. Fratzl, Cooperative Deformation of Mineral and Collagen in Bone at the Nanoscale, 2006.
[96] A. Groetsch, P.K. Zysset, P. Varga, A. Pacureanu, F. Peyrin, U. Wolfram, Sci. Rep. 11 (2021).
[97] G.R. Jordan, N. Loveridge, J. Power, M.T. Clarke, J. Reeve, Osteoporos. Int. 14 (2003) 160–165.
[98] A.C. Vale, M.F.C. Pereira, A. Maurício, B. Vidal, A. Rodrigues, J. Caetano-Lopes, A. Nazarian, J.E. Fonseca, H. Canhão, M.F. Vaz, J. Biomed. Sci. Eng. 06 (2013) 175–184.
[99] D.E. Hurwitz, K.C. Foucher, D.R. Sumner, T.P. Andriacchi, A.G. Rosenberg, J. O. Galante, Hip Motion and Moments during Gait Relate Directly to Proximal Femoral Bone Mineral Density in Patients with Hip Osteoarthritis, 1998.
[100] C. De Laet, A. Odén, H. Johansson, O. Johnell, B. Jönsson, J.A. Kanis, Osteoporos. Int. 16 (2005) 313–318.
[101] J.H. Lin, Bone 18 (1996) 75–85.
[102] C. Deng, J.C. Gillette, T.R. Derrick, PLoS One 16 (2021) 1–14.
[103] M.E. Kersh, S. Martelli, R. Zebaze, E. Seeman, M.G. Pandy, J. Bone Miner. Res. 33 (2018) 1999–2006.
[104] S.J. Edmondston, K.P. Singer, R.E. Day, P.D. Breidahl, R.I. Price, Clin. Biomech. 9 (1994) 175–179.
[105] K.J. Burkhart, T.E. Nowak, J. Blum, S. Kuhn, M. Welker, W. Sternstein, L. P. Mueller, P.M. Rommens, Biomed. Tech. 55 (2010) 361–365.
[106] F. Faul, E. Erdfelder, A.-G. Lang, A. Buchner, Behav. Res. Methods 39 (2007) 175–191.